Numerical Modeling of Coupled Water Flow and Heat Transport in Soil and Snow

Thijs J. Kelleners*
Dep. of Ecosystem Science and Management
Univ. of Wyoming
Laramie, WY 82071

Jeremy Koonce
Rose Shillito
Jelle Dijkema
Markus Berli
Division of Hydrologic Sciences
Desert Research Institute
Las Vegas, NV 89119

Michael H. Young
Bureau of Economic Geology
Univ. of Texas
Austin, TX 78758

John M. Frank
W.J. Massman
US Forest Service
Rocky Mountain Research Station
Fort Collins, CO 80526

A one-dimensional vertical numerical model for coupled water flow and heat transport in soil and snow was modified to include all three phases of water: vapor, liquid, and ice. The top boundary condition in the model is driven by incoming precipitation and the surface energy balance. The model was applied to three different terrestrial systems: a warm desert bare lysimeter soil in Boulder City, NV; a cool mixed-grass rangeland soil near Laramie, WY; and a snow-dominated mountainous forest soil about 50 km west of Laramie, WY. Comparison of measured and calculated soil water contents with depth yielded modeling efficiency (ME) values (maximum range: $-\infty < \text{ME} \leq 1$) of $0.32 \leq \text{ME} \leq 0.75$ for the bare soil, $0.05 \leq \text{ME} \leq 0.30$ for the rangeland soil, and $0.06 \leq \text{ME} \leq 0.37$ for the forest soil. Results for soil temperature with depth were $0.87 \leq \text{ME} \leq 0.91$ for the bare soil, $0.92 \leq \text{ME} \leq 0.94$ for the rangeland soil, and $0.85 \leq \text{ME} \leq 0.88$ for the forest soil. The model described the mass change in the bare soil lysimeter due to outgoing evaporation with moderate accuracy (ME = 0.41, based on 4 yr of data and using weekly evaporation rates). Snow height for the rangeland soil and the forest soil was captured reasonably well (ME = 0.57 for both sites based on 5 yr of data for each site). The model is physics based, with few empirical parameters, making it applicable to a wide range of terrestrial ecosystems.

Abbreviations: LAI, leaf area index; ME, modeling efficiency.

Core Ideas

- **Models of coupled water flow and heat transport improve our understanding of ecosystems.**
- **Soil and snow liquid water flow, water vapor flow, and ice are described using numerical models.**
- **The model is verified for a bare desert soil, a rangeland soil, and a forest soil.**

The ability to understand and quantify temporal dynamics in water and heat storage in soil and snow is important across a range of terrestrial ecosystems. The modeling of water and heat fluxes in the soil–plant–atmosphere system is used in many disciplines such as agriculture, structural engineering, hydrology, ecology, and climate science. Increasingly detailed algorithms on water and heat exchange are now also routinely included in watershed- and basin-scale computer simulation models to improve regional water management. The effect of climate change and land use change on modifying water and heat fluxes are a particularly active area of research at present.

Water in soil and snow is stored in three phases: liquid, vapor, and solid (ice). Water flow and heat transport are coupled processes. For example, vaporizing liquid water requires heat and freezing liquid water releases heat as the water molecules are moved to a higher and lower energy state, respectively. Soil salinity influences the vaporization and freezing processes by lowering the energy state of the liquid water, reducing vaporization rates, and delaying the onset of freezing. Soil type has a similar effect, with fine-textured soils having higher water retention thus reducing the energy state of the water.

The theory of water flow, heat transport, and phase change in soil and snow has been worked out during the past decades. Philip and de Vries (1957) showed how liquid water and water vapor transfer may be separated into isothermal and thermal components. Guymon and Luthin (1974) used the Clapeyron equation

---

Soil Sci. Soc. Am. J. 80:247–263
doi:10.2136/sssaj2015.07.0279
Received 3 Aug. 2015.
Accepted 9 Dec. 2015.
*Corresponding author (tkellene@uwyo.edu).

and the soil water retention curve to relate freezing temperature to liquid water potential and liquid water content in frozen soils. Fuchs et al. (1978) incorporated the effect of osmotic potential into the relationship between freezing temperature and water potential in frozen soil. Nassar and Horton (1989) added osmotic effects to the relationship between soil liquid water potential and soil air relative humidity.

The calculation of water flow and heat transport in soil and snow generally requires numerical techniques due to the heterogeneous nature of the media and the variable boundary condition with the atmosphere. Root water uptake further complicates matters. Early models treated water flow and heat transport separately and neglected vapor and ice. Subsequent models incorporated either water vapor flow (Fayer, 2000; Saito et al., 2006) or freezing (Harlan, 1973; Dall'Amico et al., 2011). Relatively few models consider all three phases of water simultaneously (Zhao et al., 1997; Hansson et al., 2004; Painter, 2011). Even fewer models treat water flow and heat transport in soil and snow with the same rigor (Flerchinger and Saxton, 1989; Flerchinger, 2000).

The purpose of this study was to develop a rigorous numerical model for coupled water flow and heat transport in soil and snow. The model is an extension of that presented by Kelleners et al. (2009), Kelleners and Verma (2012), and Kelleners (2013). The earlier versions of the model included only water phase change due to freeze–thaw. The new model now also includes water vapor flow. The canopy and surface energy balance, as explained in the previous studies, remains largely unchanged, including the ability to calculate incoming solar radiation in complex terrain. Within-canopy transfer of sensible and latent heat was modified for this study by using an exponential wind profile as proposed by Dolman (1993). Soil evaporation and root water uptake were modified based on recent studies by Tang and Riley (2013) and de Jong van Lier et al. (2008), respectively. The effect of ion concentration on coupled flow and transport was incorporated by assuming that the solute mass in the soil profile is time invariant, with solute concentration increasing (decreasing) as the soil water content decreases (increases).

The specific objectives of the study were: (i) to develop the coupled water flow and heat transport equations for soil and snow; (ii) to apply the model to a warm-climate bare soil where water vapor flow might be relatively significant; (iii) to apply the model to a cold-climate rangeland soil where soil freezing is significant; and (iv) to apply the model to a cold-climate mountainous forest soil where snow accumulation and melt dominate the annual hydrological cycle. With the first case (bare soil contained in a lysimeter), the lysimeter weight change was used to verify the calculated water fluxes due to incoming precipitation and outgoing soil evaporation. In addition, calculated water and heat fluxes were validated indirectly by comparing the measured and calculated soil water contents and soil temperatures. For the other two cases, no direct flux measurements were available and the calculated water and heat fluxes were both validated indirectly by determining the model's ability to replicate the measured soil water contents, soil temperatures, and snow height dynamics.

THEORY

The main water flow and heat transport equations are provided in this section as well as a description of the updated calculation methods for within canopy transfer, soil evaporation, and root water uptake. Expressions for the non-zero derivative terms used are given in the appendix. The coupled water flow and heat transport equations are solved using flexible time stepping, where the time step is decreased (increased) as the number of iterations needed to solve the equations increases (decreases) following Šimůnek et al. (2013).

Snow Water Flow

Water movement in snow is the result of liquid water flow due to gravity and water vapor flow due to a temperature gradient (Colbeck and Davidson, 1973; Colbeck, 1993; Pinzer et al., 2012):

$$\frac{\partial\theta_{\mathrm{w}}}{\partial t}+\frac{1}{\rho_{\mathrm{w}}}\frac{\partial\left(\rho_{\mathrm{vs}}\theta_{\mathrm{a}}\right)}{\partial t}+\frac{\rho_{\mathrm{i}}}{\rho_{\mathrm{w}}}\frac{\partial\theta_{\mathrm{i}}}{\partial t}=\frac{\partial}{\partial z}\left(K_{\mathrm{ws}}S_{\mathrm{e}}^{3}+K_{\mathrm{vT}}\frac{\partial T}{\partial z}\right) \qquad [1]$$

where θ_{w} is liquid water content (m^3 m^{-3}), θ_{a} is air content (m^3 m^{-3}), θ_{i} is ice content (m^3 m^{-3}), ρ_{w} is liquid water density (kg m^{-3}), ρ_{vs} is saturated water vapor density (kg m^{-3}), ρ_{i} is ice density (kg m^{-3}), t is time (s), S_{e} is relative saturation (dimensionless), K_{ws} is saturated snow hydraulic conductivity (m s^{-1}), K_{vT} is thermal water vapor hydraulic conductivity (m^2 s^{-1} K^{-1}), T is temperature (°C), and z is the vertical coordinate (m). It is assumed that snow water vapor is always at saturation (e.g., Oleson et al., 2013). The relative saturation of liquid water in snow is (Jordan, 1991)

$$S_{\mathrm{e}}=\frac{\theta_{\mathrm{w}}-\theta_{\mathrm{wr}}}{1-\theta_{\mathrm{wr}}} \qquad [2]$$

where θ_{wr} is the residual liquid water content (m^3 m^{-3}) given as (Tarboton and Luce, 1996)

$$\theta_{\mathrm{wr}}=\frac{F_{\mathrm{c}}\rho_{\mathrm{sn}}}{\rho_{\mathrm{w}}} \qquad [3]$$

where $F_{\mathrm{c}} = 0.02$ is the mass of liquid water that can be retained per mass of dry snow (kg kg^{-1}), and the snow bulk density ρ_{sn} (kg m^{-3}) is calculated as

$$\rho_{\mathrm{sn}}=\theta_{\mathrm{w}}\rho_{\mathrm{w}}+\theta_{\mathrm{i}}\rho_{\mathrm{i}} \qquad [4]$$

The snow hydraulic conductivities are (Shimizu, 1970; Colbeck, 1993)

$$K_{\mathrm{ws}}=0.077\frac{\rho_{\mathrm{w}}g}{\eta}d_{\mathrm{gr}}^{2}\exp\left(\frac{-7.8\rho_{\mathrm{sn}}}{\rho_{\mathrm{w}}}\right) \qquad [5a]$$

$$K_{\mathrm{vT}}=\frac{D}{\rho_{\mathrm{w}}}\frac{\mathrm{d}\rho_{\mathrm{vs}}}{\mathrm{d}T} \qquad [5b]$$

where g is acceleration due to gravity (m s^{-2}), η is liquid water viscosity (kg m^{-1} s^{-1}), d_{gr} is snow grain diameter (m), and D is water vapor diffusivity (m^2 s^{-1}). The grain diameter for each snow layer is calculated as a function of snow temperature, snow liquid water content, and snow age (Kelleners et al., 2009). The vapor diffusivity in snow is calculated by assuming that vapor movement is unobstructed by ice (or liquid water) and that there is no diffusion enhancement, based on experimental data and theoretical considerations presented by Pinzer et al. (2012), so that

$$D=D_{\mathrm{a}} \qquad [6]$$

where D_{a} is the diffusivity of water vapor in bulk air ($\mathrm{m}^2\ \mathrm{s}^{-1}$). Use of $\theta_{\mathrm{a}} = 1 - \theta_{\mathrm{i}} - \theta_{\mathrm{w}}$, application of the product rule, and rearrangement of Eq. [1] results in the following mass balance equation:

$$\left(1-\frac{\rho_{\mathrm{vs}}}{\rho_{\mathrm{w}}}\right)\frac{\partial\theta_{\mathrm{w}}}{\partial t}+\left(\frac{\rho_{\mathrm{i}}}{\rho_{\mathrm{w}}}-\frac{\rho_{\mathrm{vs}}}{\rho_{\mathrm{w}}}\right)\frac{\partial\theta_{\mathrm{i}}}{\partial t}+\frac{\theta_{\mathrm{a}}}{\rho_{\mathrm{w}}}\frac{\partial\rho_{\mathrm{vs}}}{\partial \mathrm{t}}= \frac{\partial}{\partial z}\left(K_{\mathrm{ws}}S_{\mathrm{e}}^{3}+K_{\mathrm{vT}}\frac{\partial T}{\partial z}\right) \qquad [7]$$

The mass balance equation is written in terms of the unknown S_{e} using the chain rule and by noting that $\mathrm{d}\theta_{\mathrm{i}}/\mathrm{d}S_{\mathrm{e}}$ and $\mathrm{d}\rho_{\mathrm{vs}}/\mathrm{d}S_{\mathrm{e}}$ are zero:

$$\left(1-\frac{\rho_{\mathrm{vs}}}{\rho_{\mathrm{w}}}\right)\frac{\mathrm{d}\theta_{\mathrm{w}}}{\mathrm{d}S_{\mathrm{e}}}\frac{\partial S_{\mathrm{e}}}{\partial t}+\left(\frac{\rho_{\mathrm{i}}}{\rho_{\mathrm{w}}}-\frac{\rho_{\mathrm{vs}}}{\rho_{\mathrm{w}}}\right)\frac{\partial\theta_{\mathrm{i}}}{\partial t}+\frac{\theta_{\mathrm{a}}}{\rho_{\mathrm{w}}}\frac{\partial\rho_{\mathrm{vs}}}{\partial \mathrm{t}}= \frac{\partial}{\partial z}\left(K_{\mathrm{ws}}S_{\mathrm{e}}^{3}+K_{\mathrm{vT}}\frac{\partial T}{\partial z}\right) \qquad [8]$$

The mass balance equation is solved for S_{e} by using the mixed formulation of Celia et al. (1990) where the three storage terms in Eq. [1] are combined with the single $\partial S_{\mathrm{e}}/\partial t$ term in Eq. [8] to describe the change in storage with time. The creation, compaction, and merger of snow layers is handled at each time step outside the numerical solution. Compaction due to metamorphism and overburden follows Jordan (1991). Snow layers that drop below a preset minimum thickness (1 cm in this study) are merged with an underlying layer. Snow layers that exceed a preset maximum thickness (2 cm in this study) are split into equal parts (Kelleners et al., 2009).

Soil Water Flow

Water movement in soil is due to pressure head gradients, temperature gradients, and gravity (the effect of gravity on water vapor is ignored). The soil water flow equation is (Hansson et al., 2004; Saito et al., 2006)

$$\frac{\partial\theta_{\mathrm{w}}}{\partial t}+\frac{1}{\rho_{\mathrm{w}}}\frac{\partial\left(H_{\mathrm{r}}\rho_{\mathrm{vs}}\theta_{\mathrm{a}}\right)}{\partial t}+\frac{\rho_{\mathrm{i}}}{\rho_{\mathrm{w}}}\frac{\partial\theta_{\mathrm{i}}}{\partial t}= \frac{\partial}{\partial z}\left(K_{\mathrm{wh}}\frac{\partial h}{\partial z}+K_{\mathrm{wh}}+K_{\mathrm{wT}}\frac{\partial T}{\partial z} +K_{\mathrm{vh}}\frac{\partial h}{\partial z}+K_{\mathrm{vT}}\frac{\partial T}{\partial z}\right)-S_{\mathrm{w}} \qquad [9]$$

where H_{r} is soil air relative humidity (dimensionless), h is soil water pressure head (m), K_{wh} is isothermal liquid water hydraulic conductivity ($\mathrm{m\ s}^{-1}$), K_{wT} is thermal liquid water hydraulic conductivity ($\mathrm{m}^2\ \mathrm{s}^{-1}\ \mathrm{K}^{-1}$), K_{vh} is isothermal water vapor hydraulic conductivity ($\mathrm{m\ s}^{-1}$), K_{vT} is thermal water vapor hydraulic conductivity ($\mathrm{m}^2\ \mathrm{s}^{-1}\ \mathrm{K}^{-1}$), and S_{w} is a sink term for root water uptake (s^{-1}). Assuming that the contributions from the pressure potential and osmotic potential are additive, and the solute is conservative, the relative humidity (as a fraction) is (Nassar and Horton, 1992)

$$H_{\mathrm{r}}=\exp\left[\frac{hM_{\mathrm{w}}g}{R(T+273.15)}-\frac{\phi}{\theta_{\mathrm{w}}}MM_{\mathrm{w}}\right],\quad h\le 0 \qquad [10]$$

where M_{w} is the molecular mass of water ($\mathrm{kg\ mol}^{-1}$), M is molality at saturation ($\mathrm{mol\ kg}^{-1}$ of solvent), R is the gas constant ($\mathrm{J\ mol}^{-1}\ \mathrm{K}^{-1}$), and ϕ is porosity ($\mathrm{m}^3\ \mathrm{m}^{-3}$). The soil hydraulic conductivities are (Hansson et al., 2004; Saito et al., 2006)

$$K_{\mathrm{wh}}=K_{\mathrm{whs}}S_{\mathrm{e}}^{\lambda}\left[1-\left(1-S_{\mathrm{e}}^{1/m}\right)^{m}\right]^{2}\times 10^{-\Omega\theta_{\mathrm{i}}} \qquad [11\mathrm{a}]$$

$$K_{\mathrm{wT}}=K_{\mathrm{wh}}hG\frac{1}{\gamma_{0}}\frac{\mathrm{d}\gamma}{\mathrm{d}T} \qquad [11\mathrm{b}]$$

$$K_{\mathrm{vh}}=D\frac{\rho_{\mathrm{vs}}}{\rho_{\mathrm{w}}}\frac{\mathrm{d}H_{\mathrm{r}}}{\mathrm{d}h} \qquad [11\mathrm{c}]$$

$$K_{\mathrm{vT}}=\frac{D}{\rho_{\mathrm{w}}}\eta_{\mathrm{e}}H_{\mathrm{r}}\frac{\mathrm{d}\rho_{\mathrm{vs}}}{\mathrm{d}T}+\frac{D}{\rho_{\mathrm{w}}}\eta_{\mathrm{e}}\rho_{\mathrm{vs}}\frac{\mathrm{d}H_{\mathrm{r}}}{\mathrm{d}T} \qquad [11\mathrm{d}]$$

where K_{whs} is saturated soil liquid water hydraulic conductivity ($\mathrm{m\ s}^{-1}$), m (dimensionless) and λ (dimensionless) are empirical parameters in the van Genuchten–Mualem soil hydraulic functions, Ω is an impedance factor (dimensionless), $G = 4$ is a gain factor (dimensionless), γ is soil water surface tension ($\mathrm{kg\ s}^{-2}$), γ_0 is soil water surface tension at 25°C ($\mathrm{kg\ s}^{-2}$), and η_{e} is an enhancement factor (dimensionless) as derived by Cass et al. (1984). Values for the impedance factor, which describes the blocking of pores due to ice formation (e.g., Hansson et al., 2004), were set to zero for all soil layers, except for the rangeland soil where $\Omega = 4.4$ was used below the 40-cm depth based on a previous model calibration (Kelleners, 2013). The soil relative saturation and water retention function are (van Genuchten, 1980)

$$S_{\mathrm{e}}=\frac{\theta_{\mathrm{w}}-\theta_{\mathrm{wr}}}{\phi-\theta_{\mathrm{wr}}}=\left(1+\left|\alpha h\right|^{n}\right)^{-m},\quad h\le 0 \qquad [12]$$

where α (m^{-1}) and n (dimensionless) are empirical parameters, with $m = 1 - 1/n$. The diffusivity of water vapor in soil is (Moldrup et al., 1999)

$$D=D_{\mathrm{a}}\theta_{\mathrm{a}}\tau=D_{\mathrm{a}}\theta_{\mathrm{a}}\frac{\theta_{\mathrm{a}}^{1+3/b}}{\phi^{3/b}} \qquad [13]$$

where τ is the tortuosity factor (dimensionless) and b is the Campbell soil water retention parameter (dimensionless) approximated as $1/(n - 1)$. The use of $\theta_{\mathrm{a}} = \phi - \theta_{\mathrm{i}} - \theta_{\mathrm{w}}$, application of the triple product rule, and rearrangement of Eq. [9] results in the following mass balance equation:

$$\left(1-\frac{H_{\mathrm{r}}\rho_{\mathrm{vs}}}{\rho_{\mathrm{w}}}\right)\frac{\partial\theta_{\mathrm{w}}}{\partial t}+\left(\frac{\rho_{\mathrm{i}}}{\rho_{\mathrm{w}}}-\frac{H_{\mathrm{r}}\rho_{\mathrm{vs}}}{\rho_{\mathrm{w}}}\right)\frac{\partial\theta_{\mathrm{i}}}{\partial t}+\frac{\rho_{\mathrm{vs}}\theta_{\mathrm{a}}}{\rho_{\mathrm{w}}}\frac{\partial H_{\mathrm{r}}}{\partial t}+\frac{H_{\mathrm{r}}\theta_{\mathrm{a}}}{\rho_{\mathrm{w}}}\frac{\partial\rho_{\mathrm{vs}}}{\partial t}=\frac{\partial}{\partial z}\left(K_{\mathrm{wh}}\frac{\partial h}{\partial z}+K_{\mathrm{wh}}+K_{\mathrm{wT}}\frac{\partial T}{\partial z}+K_{\mathrm{vh}}\frac{\partial h}{\partial z}+K_{\mathrm{vT}}\frac{\partial T}{\partial z}\right)-S_{\mathrm{w}} \qquad [14]$$

The mass balance equation is written in terms of the unknown h using the chain rule and by noting that $\mathrm{d}\rho_{\mathrm{vs}}/\mathrm{d}h$ is zero:

$$\left(1-\frac{H_{\mathrm{r}}\rho_{\mathrm{vs}}}{\rho_{\mathrm{w}}}\right)\frac{\mathrm{d}\theta_{\mathrm{w}}}{\mathrm{d}h}\frac{\partial h}{\partial t}+\left(\frac{\rho_{\mathrm{i}}}{\rho_{\mathrm{w}}}-\frac{H_{\mathrm{r}}\rho_{\mathrm{vs}}}{\rho_{\mathrm{w}}}\right)\frac{\mathrm{d}\theta_{\mathrm{i}}}{\mathrm{d}h}\frac{\partial h}{\partial t}+\frac{\rho_{\mathrm{vs}}\theta_{\mathrm{a}}}{\rho_{\mathrm{w}}}\frac{\mathrm{d}H_{\mathrm{r}}}{\mathrm{d}h}\frac{\partial h}{\partial t}+\frac{H_{\mathrm{r}}\theta_{\mathrm{a}}}{\rho_{\mathrm{w}}}\frac{\partial\rho_{\mathrm{vs}}}{\partial t}=\frac{\partial}{\partial z}\left(K_{\mathrm{wh}}\frac{\partial h}{\partial z}+K_{\mathrm{wh}}+K_{\mathrm{wT}}\frac{\partial T}{\partial z}+K_{\mathrm{vh}}\frac{\partial h}{\partial z}+K_{\mathrm{vT}}\frac{\partial T}{\partial z}\right)-S_{\mathrm{w}} \qquad [15]$$

The mass balance equation is solved for h by using the mixed formulation of Celia et al. (1990), where the three storage terms in Eq. [9] are combined with the three $\partial h/\partial t$ terms in Eq. [15] to describe the change in storage with time. Note that $\mathrm{d}\theta_{\mathrm{i}}/\mathrm{d}h = -\mathrm{d}\theta_{\mathrm{w}}/\mathrm{d}h$ for saturated frozen soils, while $\mathrm{d}\theta_{\mathrm{i}}/\mathrm{d}h = 0$ for unsaturated soils. This avoids the need for a separate water flow equation for saturated frozen conditions, as was used by Kelleners (2013).

Snow–Soil Heat Transport

Heat transport is due to conduction and convection and is calculated using (Hansson et al., 2004; Saito et al., 2006)

$$\frac{\partial(CT)}{\partial t}+\gamma_{\mathrm{v}}\frac{\partial(H_{\mathrm{r}}\rho_{\mathrm{vs}}\theta_{\mathrm{a}})}{\partial t}-\gamma_{\mathrm{f}}\rho_{\mathrm{i}}\frac{\partial\theta_{\mathrm{i}}}{\partial t}=\frac{\partial}{\partial z}\left(\kappa\frac{\partial T}{\partial z}-C_{\mathrm{w}}q_{\mathrm{w}}T-c_{\mathrm{v}}\rho_{\mathrm{w}}q_{\mathrm{v}}T-\gamma_{\mathrm{v}}\rho_{\mathrm{w}}q_{\mathrm{v}}\right)-C_{\mathrm{w}}S_{\mathrm{w}}T \qquad [16]$$

where C is bulk snow-soil heat capacity (J m^{-3} K^{-1}), γ_{v} is latent heat of vaporization (J kg^{-1}), γ_{f} is latent heat of fusion (J kg^{-1}), κ is bulk snow–soil thermal conductivity (J m^{-1} s^{-1} K^{-1}), C_{w} is liquid water heat capacity (J m^{-3} K^{-1}), c_{v} is water vapor heat capacity (J kg^{-1} K^{-1}), q_{w} is liquid water flux (m s^{-1}), and q_{v} is water vapor flux (expressed as an equivalent liquid water flux, m s^{-1}). Note that $H_{\mathrm{r}} = 1$ for snow and $0 \leq H_{\mathrm{r}} \leq 1$ for soil. The snow and soil volumetric heat capacities are, respectively,

$$C=\theta_{\mathrm{w}}C_{\mathrm{w}}+\theta_{\mathrm{i}}C_{\mathrm{i}}+\theta_{\mathrm{a}}C_{\mathrm{a}} \qquad [17a]$$

$$C=(1-\phi)C_{\mathrm{s}}+\theta_{\mathrm{w}}C_{\mathrm{w}}+\theta_{\mathrm{i}}C_{\mathrm{i}}+\theta_{\mathrm{a}}C_{\mathrm{a}} \qquad [17b]$$

where C_{i} is heat capacity of ice (J m^{-3} K^{-1}), C_{a} is heat capacity of air (J m^{-3} K^{-1}), and C_{s} is heat capacity of solids (J m^{-3} K^{-1}). The snow and soil thermal conductivities are, respectively (Jordan, 1991; Farouki, 1981),

$$\kappa=\kappa_{\mathrm{a}}+\left(7.75\times10^{-5}\rho_{\mathrm{sn}}+1.105\times10^{-6}\rho_{\mathrm{sn}}^{2}\right)\times\left(\kappa_{\mathrm{i}}-\kappa_{\mathrm{a}}\right) \qquad [18a]$$

$$\kappa=\kappa_{\mathrm{dry}}+F_{\mathrm{KN}}\left(\kappa_{\mathrm{sat}}-\kappa_{\mathrm{dry}}\right) \qquad [18b]$$

where κ_{a} is thermal conductivity of air (J m^{-1} s^{-1} K^{-1}), κ_{i} is thermal conductivity of ice (J m^{-1} s^{-1} K^{-1}), κ_{dry} is thermal conductivity of dry soil (J m^{-1} s^{-1} K^{-1}), κ_{sat} is thermal conductivity of saturated soil (J m^{-1} s^{-1} K^{-1}), and F_{KN} is the Kersten number (dimensionless). The Kersten number is a function of the degree of saturation and the phase of water (Oleson et al., 2013). Application of the triple product rule and the volume relationship $\mathrm{d}\theta_{\mathrm{i}} = -\mathrm{d}\theta_{\mathrm{w}}$ results in

$$\frac{\partial(CT)}{\partial t}+\gamma_{\mathrm{v}}\rho_{\mathrm{vs}}\theta_{\mathrm{a}}\frac{\partial H_{\mathrm{r}}}{\partial t}+\gamma_{\mathrm{v}}H_{\mathrm{r}}\theta_{\mathrm{a}}\frac{\partial\rho_{\mathrm{vs}}}{\partial t}+\gamma_{\mathrm{v}}H_{\mathrm{r}}\rho_{\mathrm{vs}}\frac{\partial\theta_{\mathrm{a}}}{\partial t}+\gamma_{\mathrm{f}}\rho_{\mathrm{i}}\frac{\partial\theta_{\mathrm{w}}}{\partial t}=\frac{\partial}{\partial z}\left(\kappa\frac{\partial T}{\partial z}-C_{\mathrm{w}}q_{\mathrm{w}}T-c_{\mathrm{v}}\rho_{\mathrm{w}}q_{\mathrm{v}}T-\gamma_{\mathrm{v}}\rho_{\mathrm{w}}q_{\mathrm{v}}\right)-C_{\mathrm{w}}S_{\mathrm{w}}T \qquad [19]$$

The energy balance equation is written in terms of the unknown T using the chain rule and by noting that $\mathrm{d}\theta_{\mathrm{a}}/\mathrm{d}T$ is zero:

$$\frac{\partial(CT)}{\partial t}+\gamma_{\mathrm{v}}\rho_{\mathrm{vs}}\theta_{\mathrm{a}}\frac{\mathrm{d}H_{\mathrm{r}}}{\mathrm{d}T}\frac{\partial T}{\partial t}+\gamma_{\mathrm{v}}H_{\mathrm{r}}\theta_{\mathrm{a}}\frac{\mathrm{d}\rho_{\mathrm{vs}}}{\mathrm{d}T}\frac{\partial T}{\partial t}+\gamma_{\mathrm{v}}H_{\mathrm{r}}\rho_{\mathrm{vs}}\frac{\partial\theta_{\mathrm{a}}}{\partial t}+\gamma_{\mathrm{f}}\rho_{\mathrm{i}}\frac{\mathrm{d}\theta_{\mathrm{w}}}{\mathrm{d}T}\frac{\partial T}{\partial t}=\frac{\partial}{\partial z}\left(\kappa\frac{\partial T}{\partial z}-C_{\mathrm{w}}q_{\mathrm{w}}T-c_{\mathrm{v}}\rho_{\mathrm{w}}q_{\mathrm{v}}T-\gamma_{\mathrm{v}}\rho_{\mathrm{w}}q_{\mathrm{v}}\right)-C_{\mathrm{w}}S_{\mathrm{w}}T \qquad [20]$$

The energy balance equation is solved for T by using the mixed formulation of Celia et al. (1990), where the three storage terms in Eq. [16] are combined with the three $\partial T/\partial t$ terms in Eq. [20] to describe the change in storage with time. Note that Kelleners (2013) used the mass relationship $\mathrm{d}\theta_{\mathrm{i}} = -\rho_{\mathrm{w}}\mathrm{d}\theta_{\mathrm{w}}/\rho_{\mathrm{i}}$ instead of the volume relationship $\mathrm{d}\theta_{\mathrm{i}} = -\mathrm{d}\theta_{\mathrm{w}}$ to eliminate θ_{i} from the heat transport equation for unsaturated frozen soils. Both options have been used in the literature (e.g., Fuchs et al., 1978; Hansson et al., 2004). The benefit of using the volume relationship for both unsaturated and saturated frozen soil conditions is that it avoids the need for a separate soil water flow equation for saturated frozen conditions. The use of either the volume or mass relationship seems to have little impact on the resulting calculations, based on limited testing. (See Kelleners [2013] for more details on the solution strategy for the coupled water flow and heat transport equations.)

Soil–Plant–Atmosphere Transfer

The model calculates the complete canopy and ground surface energy balance by solving for the canopy and ground surface temperatures, respectively (complete equation set given in Kelleners et al. [2009] and Kelleners and Verma [2012]). Previously, the surface resistance to soil evaporation was ignored and the latent and sensible heat flux between the soil surface and the canopy air was calculated by weighing the transfer coefficients of bare ground and shaded ground (e.g., Oleson et al., 2013). For the current study, the conductance factors that govern the exchange of latent and sensible heat in the soil–plant–atmosphere system were updated in two significant ways: First, soil evaporation is now regulated by conductance factors for liquid water flow and water vapor flow (acting in parallel) in the upper half of the top soil element to describe surface resistance. Second, the transfer of water vapor and heat in the canopy air space is now calculated by assuming an exponential wind profile *within* the canopy. Above-canopy transfer continues to be based on a logarithmic wind profile. The conductance factors are depicted in Fig. 1 for vegetated and unvegetated surfaces. Soil water vapor flow conductance Γ_v (m s^{-1}) and soil liquid water flow conductance Γ_w (m s^{-1}) are calculated following Tang and Riley (2013):

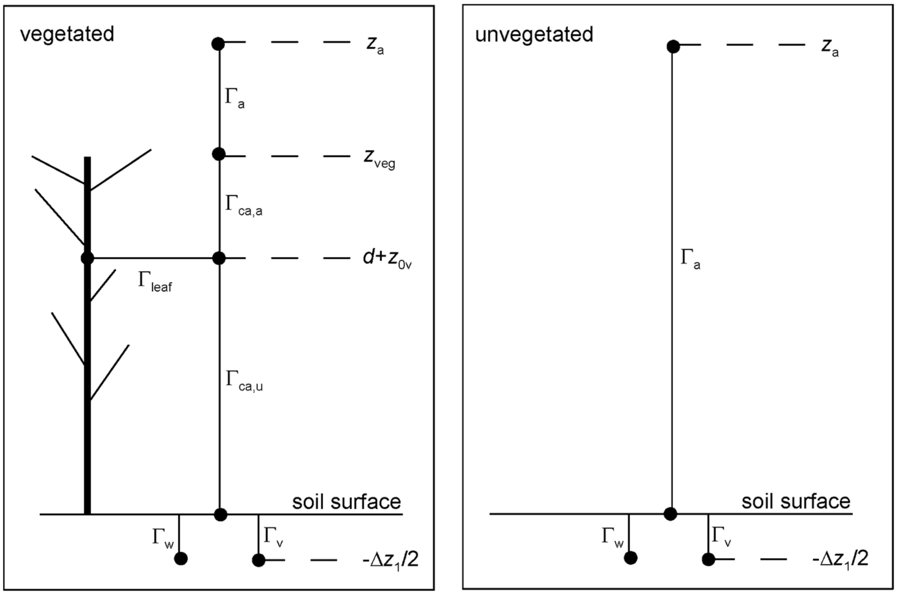

Fig. 1. Conductance factors (in m s^{-1}) for soil–plant–atmosphere latent and sensible heat exchange for vegetated and unvegetated surfaces. The conductance factors for soil liquid water flow Γ_w and soil water vapor flow Γ_v describe diffusive transport according to Tang and Riley (2013). The canopy conductance factors $\Gamma_{ca,u}$ and $\Gamma_{ca,a}$ are based on an exponential wind profile as suggested by Dolman (1993). The atmosphere conductance factor Γ_a is based on the standard logarithmic wind profile (e.g., Oleson et al., 2013). The leaf boundary conductance Γ_{leaf} is derived using the within-canopy exponential wind profile (Mahat et al., 2013). All heights are relative to the soil surface, where Δz_1 is the thickness of the topsoil element, $d + z_{0v}$ is the sum of the zero displacement height and the vegetation roughness length, z_{veg} is the vegetation height, and z_a is the height at which the meteorological input data are measured.

$$\Gamma_v = \frac{2D}{\Delta z_1} \qquad [21a]$$

$$\Gamma_w = \frac{2K_{wh}\left(\mathrm{d}h/\mathrm{d}\theta_w\right)}{\Delta z_1}\frac{\rho_w}{H_r\rho_{vs}} \qquad [21b]$$

where Δz_1 is thickness of the top soil element (m). A downside of these soil conductance factors is their dependence on the spatial discretization of the surface (the Δz_1 term). This implies that the calculated latent heat flux will be influenced in part by the top soil element thickness. This effect is at least partly offset by the fact that the diffusion terms D and $K_{wh}\mathrm{d}h/\mathrm{d}\theta_w$ for the topsoil can be expected to increase (decrease) as Δz_1 increases (decreases) in a drying soil, thus partly compensating for the Δz_1 dependency. The conductance factors for canopy air transfer $\Gamma_{ca,u}$ (lower canopy, m s^{-1}) and $\Gamma_{ca,a}$ (higher canopy, m s^{-1}) are calculated using an exponential wind profile following Dolman (1993):

$$\Gamma_{ca,u} = \frac{n_e D_{e,z_{veg}}}{\exp(n_e)z_{veg}} \times\left\{\exp\left(\frac{-n_e z_{0g}}{z_{veg}}\right) - \exp\left[\frac{-n_e\left(d+z_{0v}\right)}{z_{veg}}\right]\right\}^{-1} \qquad [22a]$$

$$\Gamma_{ca,a} = \frac{n_e D_{e,z_{veg}}}{z_{veg}}\left(\exp\left\{n_e\left[1-\frac{d+z_{0v}}{z_{veg}}\right]\right\}-1\right)^{-1} \qquad [22b]$$

where n_e is a dimensionless eddy decay coefficient (3.0 for grass and 6.0 for coniferous forest in this study), $D_{e,zveg}$ is an eddy diffusion coefficient (m^2 s^{-1}) at canopy height z_{veg} (m), z_{0g} is ground momentum roughness length (m), d is zero-plane displacement height (m), and z_{0v} is roughness length for vegetation (m, assumed the same for momentum, sensible heat, and latent heat). The conductance factor for atmospheric transfer Γ_a (m s^{-1}) is calculated using a logarithmic wind profile (Dolman, 1993):

$$\Gamma_a = \begin{cases} \dfrac{k^2 v_a \phi_{Ri}}{\ln\left[\left(z_a-d\right)/z_{0v}\right]\ln\left[\left(z_a-d\right)/\left(z_{veg}-d\right)\right]} & \text{vegetated} \\ \dfrac{k^2 v_a \phi_{Ri}}{\ln\left(z_a/z_{0g}\right)\ln\left(z_a/z_{0g,w}\right)} & \text{unvegetated} \end{cases} \qquad [23]$$

where $k = 0.4$ is the von Karman constant (dimensionless), v_a is measured wind speed above the canopy (m s^{-1}), ϕ_{Ri} atmospheric stability correction factor (dimensionless), z_a is the wind speed measurement height (m), and $z_{0g,w}$ is ground roughness length for latent heat (m). The atmospheric stability factor ϕ_{Ri} is calculated from the dimensionless Richardson number Ri as (Moene and van Dam, 2014)

$$\phi_{\mathrm{Ri}}=\begin{cases}(1-16\mathrm{Ri})^{0.75} & \text{unstable} \quad \mathrm{Ri}<0 \\ (1-5\mathrm{Ri})^{2} & \text{stable} \quad 0\le\mathrm{Ri}<0.16\end{cases} \qquad [24]$$

where 0.16 is the maximum allowed value of Ri (Mahat et al., 2013). Finally, the leaf boundary conductance Γ_{leaf} (m s^{-1}) is given by (Mahat et al., 2013)

$$\Gamma_{\mathrm{leaf}}=\frac{0.02}{n_{\mathrm{e}}}\sqrt{\frac{v_{z_{\mathrm{veg}}}}{d_{\mathrm{leaf}}}}\left[1-\exp\left(\frac{-n_{\mathrm{e}}}{2}\right)\right] \qquad [25]$$

where 0.02 has the unit of m s$^{-0.5}$, v_{zveg} is the wind speed at the canopy height (m s^{-1}), and d_{leaf} is the characteristic dimension of the leaves in the direction of wind flow (= 0.04 m in this study). Adjustments are made to the conductance factors when the ground is covered with snow. For example, $z_{0\mathrm{g}}$ in Eq. [22a] is replaced by $z_{\mathrm{snow}} + z_{0\mathrm{g}}$ to account for the snow height z_{snow}, with the assumption that the decay coefficient n_{e} remains unchanged. Also, z_{a} in Eq. [23] (unvegetated) is replaced by $z_{\mathrm{a}} - z_{\mathrm{snow}}$ when the snow completely covers the vegetation, as might happen with grass. Note that alternative methods for calculating soil evaporation exist based on pore-scale analysis of the evaporation process (e.g., Or et al., 2012). The macroscopic approach of Tang and Riley (2013) was used here because of its simplicity and because no additional parameters are needed. Other methods may be implemented in the future.

Root Water Uptake

Previous versions of the model described root water uptake through a combination of the Vrugt et al. (2001) root depth distribution function and the Feddes et al. (1978) soil water pressure head based root water uptake reduction function (Kelleners and Verma, 2012). In this new model, the sink term for root water uptake is derived from the microscopic single root analysis of de Jong van Lier et al. (2008). Their analysis allows for compensated root water uptake and hydraulic lift, two potentially important processes that were not captured by the older models. The sink term in the new model is defined as

$$S_{\mathrm{w}}=\frac{4\left(M_{\mathrm{avg}}-M_{0}\right)}{R_{0}^{2}-a^{2}R_{1}^{2}+2\left(R_{0}+R_{1}\right)^{2}\ln\left(aR_{1}/R_{0}\right)} \qquad [26]$$

where M_{avg} is matric flux potential at the average water content of the soil layer (m^2 s^{-1}), M_0 is matric flux potential at the root surface (m^2 s^{-1}), $R_0 = 3 \times 10^{-4}$ m is root radius (m), R_1 is half the mean distance between individual roots (m), and $a = 0.53$ is relative distance from the root where the water content is equal to the layer average (dimensionless). The matric flux potentials M are defined as

$$M=\int_{h_{\mathrm{wp}}}^{h}K_{\mathrm{wh}}(h)\,\mathrm{d}h \qquad [27]$$

where h_{wp} is pressure head at the permanent wilting point (m). The half mean distance between individual roots is calculated as

$$R_{1}=\frac{1}{\sqrt{\pi L}} \qquad [28]$$

where L is root length density (m m^{-3}). The values for a, R_0, and M_0 are the same for all soil layers. Analytical expressions for calculating the matric flux potential were given by de Jong van Lier et al. (2009). The root length density is calculated using the Vrugt et al. (2001) root depth distribution function. Root water uptake is calculated in several steps. First, the maximum root water uptake is calculated using $M_0 = 0$ in Eq. [26]. Then the potential transpiration rate is calculated based on the canopy energy balance (Kelleners and Verma, 2012), assuming zero water stress. Finally, the value of M_0 is calculated by comparing the maximum root water uptake and potential transpiration. A value of $M_0 = 0$ is used during periods of water stress when root water uptake cannot supply enough water to satisfy the atmospheric demand. This has the effect of maxing out the root water uptake for a given value of M_{avg}. In contrast, values of $M_0 > 0$ are calculated when there is sufficient water in the root zone.

BARE SOIL LARGE WEIGHING LYSIMETER EXPERIMENT

The numerical model was tested for bare soil conditions using 4 yr of data (October 2008– September 2012) from Lysimeter 2 of the Desert Research Institute Scaling Environmental Processes in Heterogeneous Arid Soils (SEPHAS) Large Weighing Lysimeter Facility in Boulder City, NV. The cylindrical lysimeter (2.26-m inner diameter, 3-m height) contains sand to loamy sand soil from nearby Eldorado Valley that was repacked to dry bulk densities and soil horizons found at the excavation site. The soil is classified as a sandy-skeletal, mixed, thermic Typic Torriorthent (Chief et al., 2009). The lysimeter was filled with air-dry soil between March and June 2008. Vegetation at the excavation site, about 5 km from the lysimeter facility, is dominated by creosote bush [*Larrea tridentata* (DC.) Coville], while no vegetation was allowed to grow in the lysimeter during the 4-yr data period. Soil physical characteristics of Lysimeter 2 are summarized in Table 1. The lysimeter is placed on a scale with an accuracy of ± 300 g (equivalent to ±0.075 mm of precipitation or evaporation). Any plant growth was re-

Table 1. Gravel content (>2-mm diameter), soil texture (<2-mm diameter), soil dry bulk density ρ_{b} (mass of soil [<2 mm-diameter] per field unit volume), electrical conductivity of the saturated paste extract EC_{e}, and soil class for Lysimeter 2 at the Desert Research Institute Large Weighing Lysimeter Facility at Boulder City, NV.

Depth	Gravel	Sand	Silt + clay	ρ_{b}	EC_{e}	Class
cm		%		g cm^{-3}	dS m^{-1}	
0–25	10	93	7	1.51	0.2	sand
25–80	15	93	7	1.45	0.3	sand
80–120	27	93	7	1.34	0.3	sand
120–160	34	91	9	1.25	1.0	sand
160–200	44	85	15	1.08	2.0	loamy sand
200–300	25	93	7	1.31	1.0	sand

moved by hand each spring and weighed. The associated plant mass was within the accuracy range of the lysimeter scale and no corrections were made to the lysimeter weight. Measured deep percolation from the bottom of the lysimeter was zero during the 4-yr study period. More details on the construction, layout, and operation of the lysimeter were provided by Chief et al. (2009).

The climate at Boulder City, NV (elevation 770 m above mean sea level), is characterized by low precipitation (141-mm annual average) and warm temperatures (13.7°C average annual minimum temperature; 25.4°C average annual maximum temperature) according to the closest Western Regional Climate Center meteorological station no. 261071. Half-hourly weather data (humidity, temperature, wind speed, atmospheric pressure, and precipitation) for the 4-yr calculation period were available from a weather station at the lysimeter facility. Fractional cloud cover was derived from the National Climatic Data Center station data for Henderson Executive Airport (about 16 km to the west of Boulder City at 750 m above mean sea level). Atmospheric turbidity data needed for the calculation of aerosol optical depth (Kelleners et al., 2009) were derived from monthly solar radiation data from Desert Rock, NV (Augustine et al., 2008).

Only the top 250 cm of soil in the lysimeter was modeled because no sensor observations were conducted below this depth. Vertical grid spacing was 1 cm throughout the modeled domain. Soil water retention parameters for all six soil layers were determined at the University of Wyoming. Water retention in the dry soil range was measured using a WP4 dew-point potentiometer (Decagon Devices). Water retention in medium wet soil ($-7 < h < -1$ m) was measured using Tempe cells and the pressure-outflow method (Dane and Hopmans, 2002a). Water retention in wet soils ($h > -1$ m) was measured using hanging water columns (Dane and Hopmans, 2002b). Repacked soil was used in all cases. Gravimetric water contents were converted to volumetric water contents using the bulk density values of the lysimeter soil layers (mass of soil [<2-mm diameter] per field unit volume; Russo [1983]; Table 1). Saturated volumetric water content as calculated for the lysimeter soil layers was also included as a data point. Optimum values for θ_{wr}, ϕ, α, and n were determined using the solver tool in Microsoft Excel. The resulting parameters are shown in Table 2. Saturated hydraulic conductivity K_{whs} was set at 100 cm d^{-1} for all soil layers based on unpublished results from tension infiltration experiments conducted by the Desert Research Institute. Finally, the exponent λ (Eq. [11a]) was fixed at 0.5 as recommended by Mualem (1976).

The top boundary condition for both water flow and heat transport was determined by the incoming precipitation and the surface energy balance (Kelleners et al., 2009). The bottom boundary condition for water flow was free drainage. The bottom boundary condition for heat transport was a prescribed temperature as measured by a Model 229 Heat Dissipation Unit (HDU, Campbell Scientific) at the 250-cm depth. Our preferred bottom boundary condition for heat transport of a zero temperature gradient did not work well because the lower part of the lysimeter is situated in an underground chamber. This setup conflicts with the assumption of an infinite soil profile and strictly vertical heat transport. This is reflected in the measured soil temperatures in the lysimeter, which show only a muted time lag with depth in response to seasonal changes in the surface energy balance. With the prescribed temperature boundary condition, the heat transport in the lower part of the lysimeter is more constrained, allowing the model to better capture the observed temperature dynamics. Initial conditions for water flow and heat transport were determined using time domain reflectometry TDR 100–CS 605 water content data (Campbell Scientific) and HDU temperature data measured at the 5- (HDU only), 10-, 25-, 50-, 75-, 100-, 150-, 200-, and 250-cm depths. No parameter optimization was conducted for this study and the model was run using only default values.

Table 2. Residual water content θ_{wr}, porosity ϕ, and the shape parameters α and n in the van Genuchten (1980) soil water retention function for the six soil layers of Lysimeter 2 at the Desert Research Institute Large Weighing Lysimeter Facility at Boulder City, NV.

Depth	θ_{wr}	ϕ	α	n
cm			cm^{-1}	
0–25	0.022	0.341	0.0373	1.567
25–80	0.027	0.294	0.0209	1.790
80–120	0.041	0.280	0.0269	1.888
120–160	0.025	0.260	0.0300	1.621
160–200	0.011	0.242	0.0870	1.283
200–300	0.032	0.337	0.0745	1.626

Measured and calculated soil water content and soil temperature are shown in Fig. 2 and 3, respectively, for the 10-, 25-, 50-, 100-, and 150-cm depths. Measured and calculated lysimeter liquid water gain and weekly bare soil evaporation are shown in Fig. 4, with the measured values being derived from the lysimeter mass change with time. Measured and calculated bare soil evaporation rates were compared only for periods without precipitation to eliminate the impact of discrepancies between rain-gauge-measured and lysimeter-captured rainfall on the calculated and measured evaporation rates, respectively. Weekly evaporation rates were preferred over daily evaporation rates to increase the signal/noise ratio in the measured evaporation rates (measurement accuracy ± 0.075 mm). The calculated liquid water gain and evaporation in Fig. 4 are shown for the complete model (top row), for the model without vapor flow ($K_{vh} = K_{vT} = 0$; middle row), and for the model without surface resistance ($\Gamma_v^{-1} = \Gamma_w^{-1} \approx 0$; bottom row).

The modeling statistics for the complete model with vapor flow and surface resistance are summarized in Table 3, where the root mean square error (RMSE) and ME are as defined by Green and Stephenson (1986). The maximum value for ME is 1. The model-calculated values are worse than simply using the measured mean when ME is <0. No modeling statistics are presented for lysimeter liquid water gain because later gain values are influenced by earlier gain values and therefore cannot be considered as independent values.

The ME values were variable for soil water content ($0.32 \le \text{ME} \le 0.75$), relatively high for soil temperature ($0.87 \le$

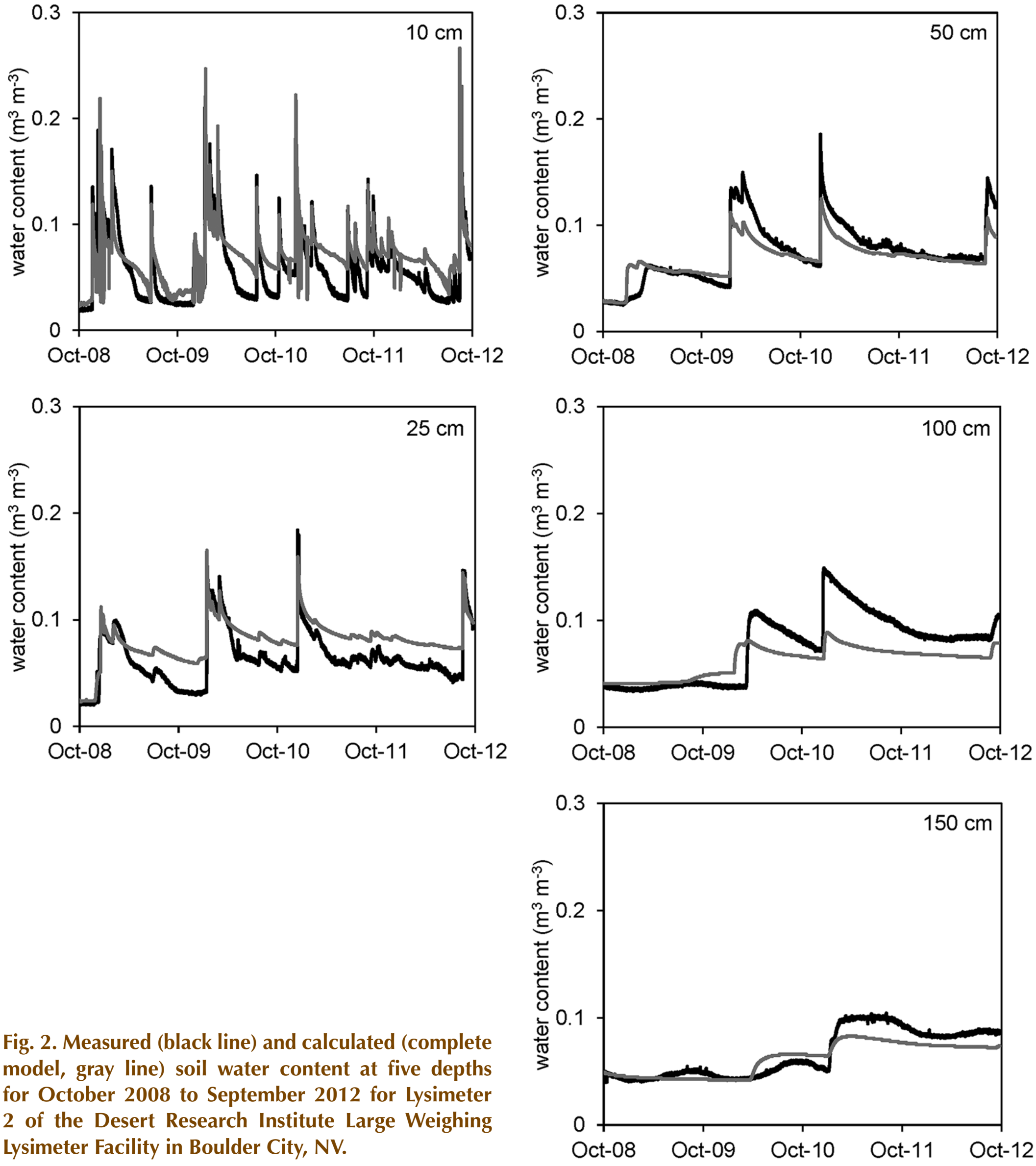

Fig. 2. Measured (black line) and calculated (complete model, gray line) soil water content at five depths for October 2008 to September 2012 for Lysimeter 2 of the Desert Research Institute Large Weighing Lysimeter Facility in Boulder City, NV.

ME $\leq$ 0.91), and intermediate for weekly bare soil evaporation (ME = 0.41). Figures 2 and 4 show that the lysimeter was gaining water while the soil moved toward a dynamic equilibrium after being packed dry between March and June 2008. In October 2012, at the end of the 4-yr simulation period, the wetting front was somewhere between the 200- and 250-cm depths (measured water contents not shown). The occasional significant dips in the calculated water contents at the 10-cm depth in Fig. 2 are due to short freezing events in winter when liquid water was transformed into ice. The two large "measured" condensation events in Fig. 4 (right column) may be due in part to missed precipitation events.

The soil temperatures were underestimated, especially during winter periods (Fig. 3). It appears that the chamber environment was keeping the measured temperatures artificially high during winter. The one-dimensional vertical model was unable to capture the true three-dimensional lysimeter environment, despite the prescribed temperatures that define the bottom boundary condition for heat transport. The change in lysimeter mass, expressed as liquid water gain in millimeters, due to incoming water from precipitation and outgoing water from evaporation was captured reasonably well by the model (Fig. 4, top left panel). The measured gain was 111 mm while the calculated gain was 95 mm during the 4-yr period. One contributing factor to the difference is that the lysimeter, with a surface area of 4 m^2, is more efficient at capturing precipitation than the rain gauge, which typically suffers from under-catch (Duchon and Biddle, 2010). A good example of this can be seen for December 2010 in Fig. 4, top left panel, when the measured liquid water gain during a period of high precipitation was significantly higher than the calculated gain.

Calculated evaporation rates for May to June were generally underestimated (Fig. 4, top right panel). This is also evident from Fig. 2, where calculated water contents at the 10- and 25-cm depths are consistently overestimated during May to June. It is difficult to determine whether these discrepancies were due to deficiencies in the surface energy balance equations, the coupled water flow–heat transport equations, the measured soil hydrau-

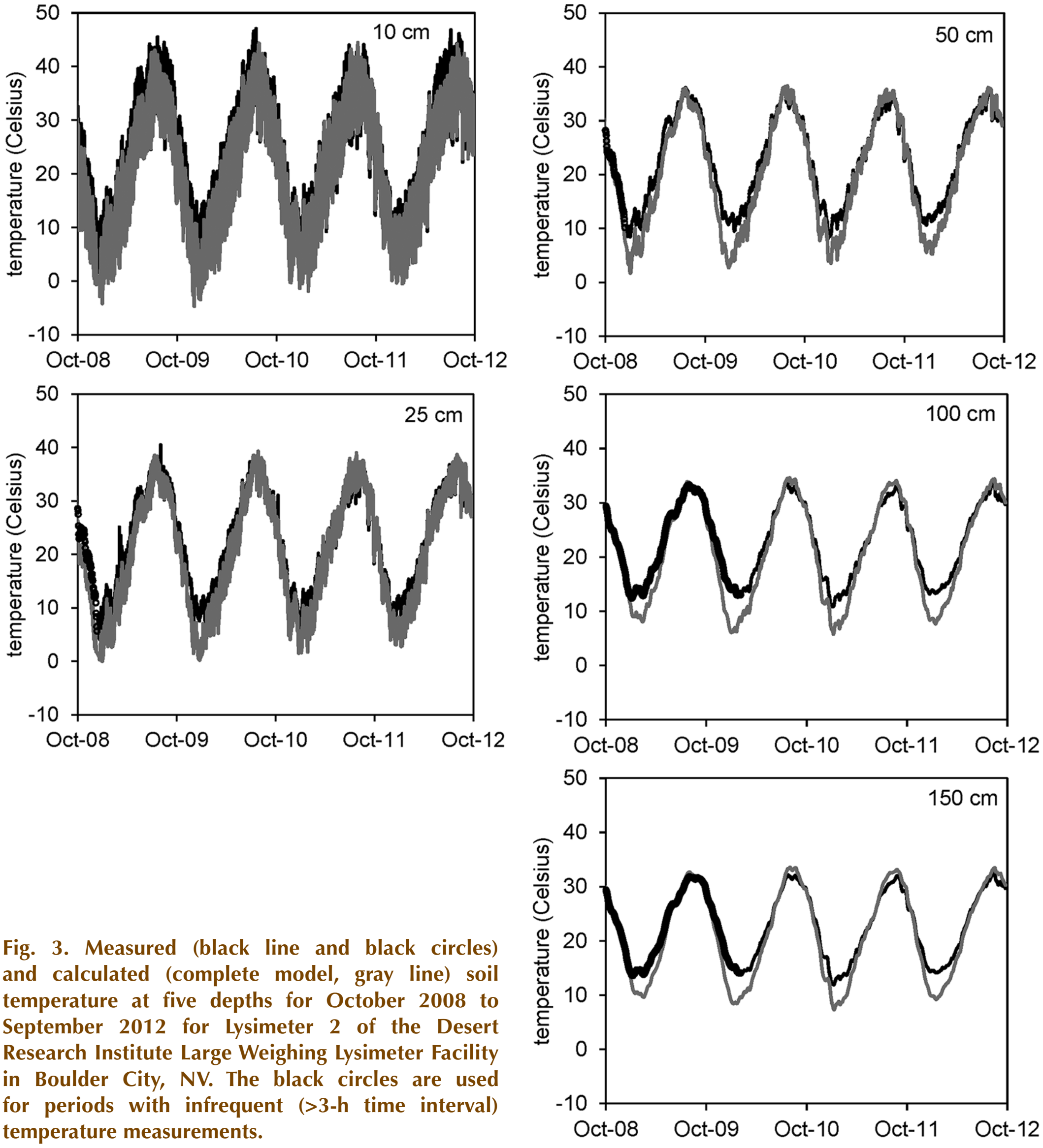

Fig. 3. Measured (black line and black circles) and calculated (complete model, gray line) soil temperature at five depths for October 2008 to September 2012 for Lysimeter 2 of the Desert Research Institute Large Weighing Lysimeter Facility in Boulder City, NV. The black circles are used for periods with infrequent (>3-h time interval) temperature measurements.

lic properties, the Tang and Riley (2013) conductance factors, or a combination of these. Exclusion of vapor flow degraded the calculated evaporation rates, with ME decreasing from 0.41 (Fig. 4, top right panel) to ME = 0.37 (Fig. 4, middle right panel). Exclusion of surface resistance also degraded the evaporation rates, with ME decreasing to 0.36 (Fig. 4, bottom right panel). In addition, the RMSE increased from 1.20 mm wk^{-1} for the complete model to 1.25 mm wk^{-1} for both cases, confirming the reduced model performance. The underestimation of May to June evaporation rates even for the case without surface resistance (Fig. 4, bottom right panel) is surprising and requires further work, which was beyond the scope of the current study.

RANGELAND SOIL FIELD EXPERIMENT

The numerical model was also applied to a semiarid mixed-grass rangeland near Laramie, WY (elevation 2200 m above sea level, average annual temperature 4.7°C, average annual precipitation 300 mm). The soil at the study site is a fine-loamy, mixed, superactive, frigid Ustic Calciargid, developed in alluvium on an old Pleistocene terrace of the Laramie River. Soil texture ranges from sandy loam for the top 10 cm to loam and sandy clay loam at depth. High percentages of $CaCO_3$ are found in the subsurface. The vegetation consists mainly of cool-season grasses and is dominated by Sandberg bluegrass (*Poa secunda* J. Presl), prairie June grass [*Koeleria macrantha* (Ledeb.) Schult.], and western wheatgrass [*Elymus smithii* (Rydb.) Barkworth and D.R. Dewey]. The site is grazed by both sheep (*Ovis aries*) and cows (*Bos taurus*) during short periods of the summer. A detailed description of the soil physical characteristics and the soil hydraulic properties for this site were provided by Kelleners and Verma (2012).

An older version of the model was applied to the same site for the July 2009 to October 2011 period (Kelleners and Verma, 2012; Kelleners, 2013). For the current study, the simulation period was extended to cover 5 yr (July 2009–September 2014). Climate data for 15-min intervals were from the Automated Surface Observation System (ASOS) at Laramie regional airport ~1 km from the site. Winter pre-

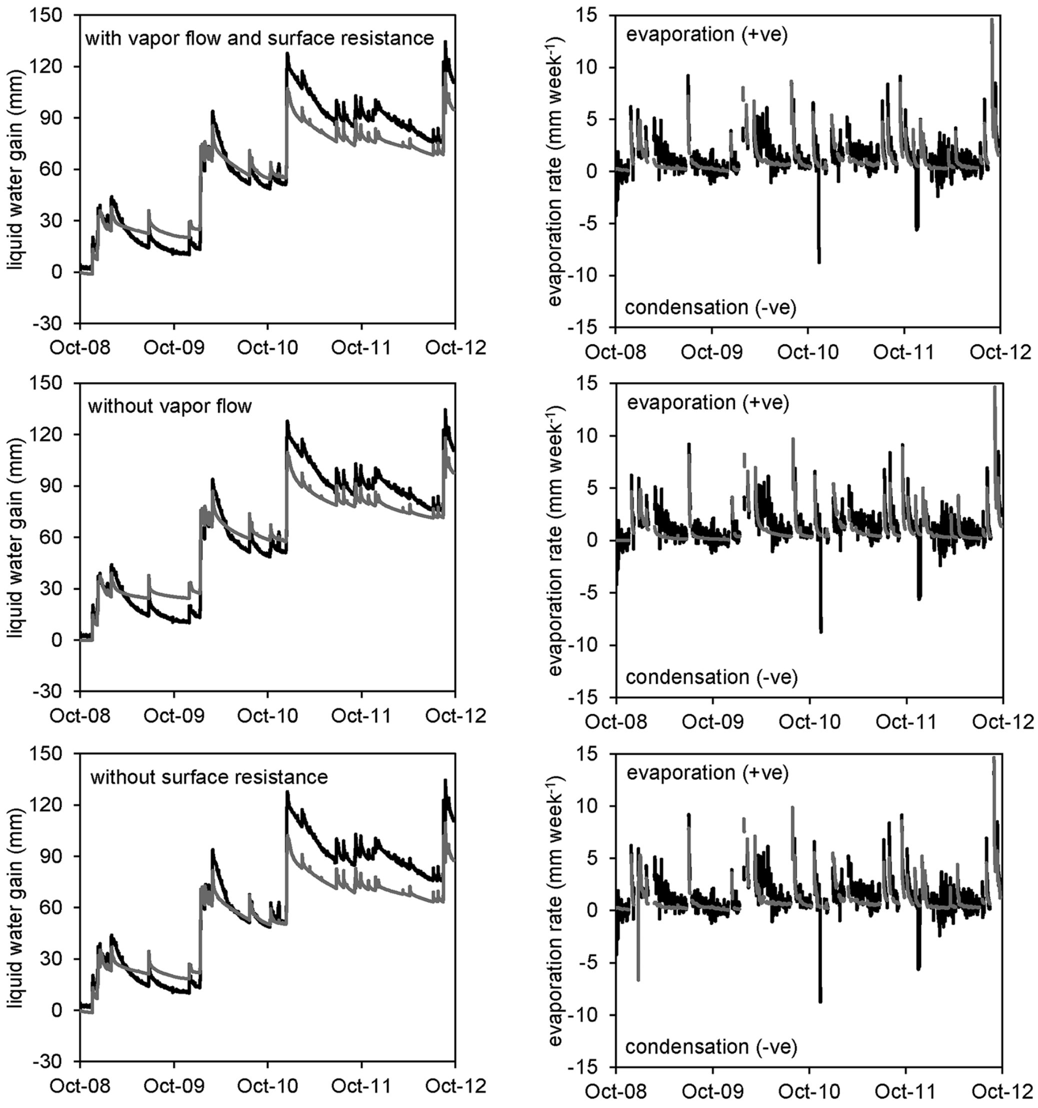

Fig. 4. Measured (black line) and calculated (gray line) liquid water gain and bare soil evaporation rate for October 2008 to September 2012 for Lysimeter 2 of the Desert Research Institute Large Weighing Lysimeter Facility in Boulder City, NV. Calculated values are shown for the complete model (top row), without vapor flow (middle row), and without surface resistance (bottom row). The measured liquid water gain and bare soil evaporation rate were derived from the lysimeter mass change with time. Measured and calculated weekly evaporation rates are shown only for periods without precipitation.

cipitation data were corrected using daily manual observations from the Community Collaborative Rain, Hail, and Snow (CoCoRaHS) network. Atmospheric turbidity was estimated from average monthly values for Cheyenne, WY, as presented by Curtis and Grimes (2004). The parameters in the Vrugt et al. (2001) root depth distribution function were changed compared with those of Kelleners and Verma (2012) to correct an error and to improve performance for the 5-yr period. The new values are: maximum rooting depth $z_m = 1.0$ m; dimensionless empirical factor $P_z = -5$; empirical parameter $z^* = 1.0$ m. In addition, a vegetation height of 0.4 m, a maximum leaf area index (LAI) of 1.7 m^2 m^{-2}, and a soil profile root mass of 1.4 kg m^{-2} was assumed (Jackson et al., 1996).

The simulated 3-m-deep soil profile had five diagnostic layers and was described using 52 nodes with grid spacing increasing from 1 cm at the surface to 50 cm in the subsurface. Soil hydraulic properties for the five layers were similar to those reported by Kelleners and Verma (2012). The top boundary condition was again the result of incoming precipitation and the surface energy balance. The bottom boundary condition for water flow was free drainage. The bottom boundary condition for heat transport was a zero temperature gradient. The initial conditions for water flow and heat transport as determined from HydraProbe impedance–temperature sensors at the 7.5-, 15-, 25-, 45-, and 65-cm depths (Stevens Water Monitoring Systems) also remained unaltered compared with the previous studies. No additional parameter optimization was conducted for the present study.

Measured and calculated soil water content, soil temperature, and snow height are shown in Fig. 5, 6, and 7, respectively, where the measured snow heights were observed manually at 30-d intervals using a meter stick. The modeling statistics are summarized in Table 4. The model performance was variable, with good performance for soil temperature ($0.92 \leq \mathrm{ME} \leq 0.94$), intermediate performance for snow height (ME = 0.57), and relatively weak performance for soil water content ($0.05 \leq \text{ME} \leq 0.30$). These modeling statistics are similar to those of our previous studies, which used only 2 yr of data (Kelleners and Verma, 2012; Kelleners, 2013). The RMSE values for soil water contents of 0.03 to 0.04 $m^3\ m^{-3}$ are only slightly above the measurement accuracy of $\pm 0.03\ m^3\ m^{-3}$ for the HydraProbe (e.g., Kammerer et al., 2014), suggesting that soil spatial heterogeneity and sensor calibration are significant contributing factors to the discrepancies between measured and calculated soil water content.

Systematic discrepancies between measured and calculated soil water content occurred mainly for the 45- and 65-cm depths (Fig. 5). The water content was generally overestimated at these depths. This was probably due to imperfections in the soil hydraulic properties (which were measured) and/or vegetation parameters (only partly based on measurements), in addition to the effects of soil spatial heterogeneity and sensor calibration as mentioned above. The calculated steep drops in (liquid) soil water content in winter were due to soil water freezing. These drops can also be observed in the measured values, albeit only when winter water contents were relatively high at the onset of freezing. Note that impedance probes, like most electromagnetic soil water content sensors, mainly react to liquid water content (relative permittivity ~80) and not so much to ice (relative permittivity ~3).

The good model performance for soil temperature (Fig. 6) suggests that the calculated canopy and surface energy balances are realistic for the mixed-grass ecosystem. Both the diurnal and seasonal trends were captured accurately. Snow

Table 3. Model statistics of root mean square error (RMSE) and modeling efficiency (ME) for soil water content, soil temperature, and the bare soil evaporation rate for October 2008 to September 2012 for Lysimeter 2 of the Desert Research Institute Large Weighing Lysimeter Facility in Boulder City, NV.

Depth	Soil water content		Soil temperature		Bare soil evaporation	
	RMSE	ME	RMSE	ME	RMSE	ME
cm	$m^3\ m^{-3}$		°C		$mm\ wk^{-1}$	
Surface					1.2	0.41
10	0.02	0.56	3.3	0.91		
25	0.02	0.32	3.0	0.89		
50	0.01	0.75	3.1	0.87		
100	0.02	0.41	2.6	0.87		
150	0.01	0.75	2.3	0.87		

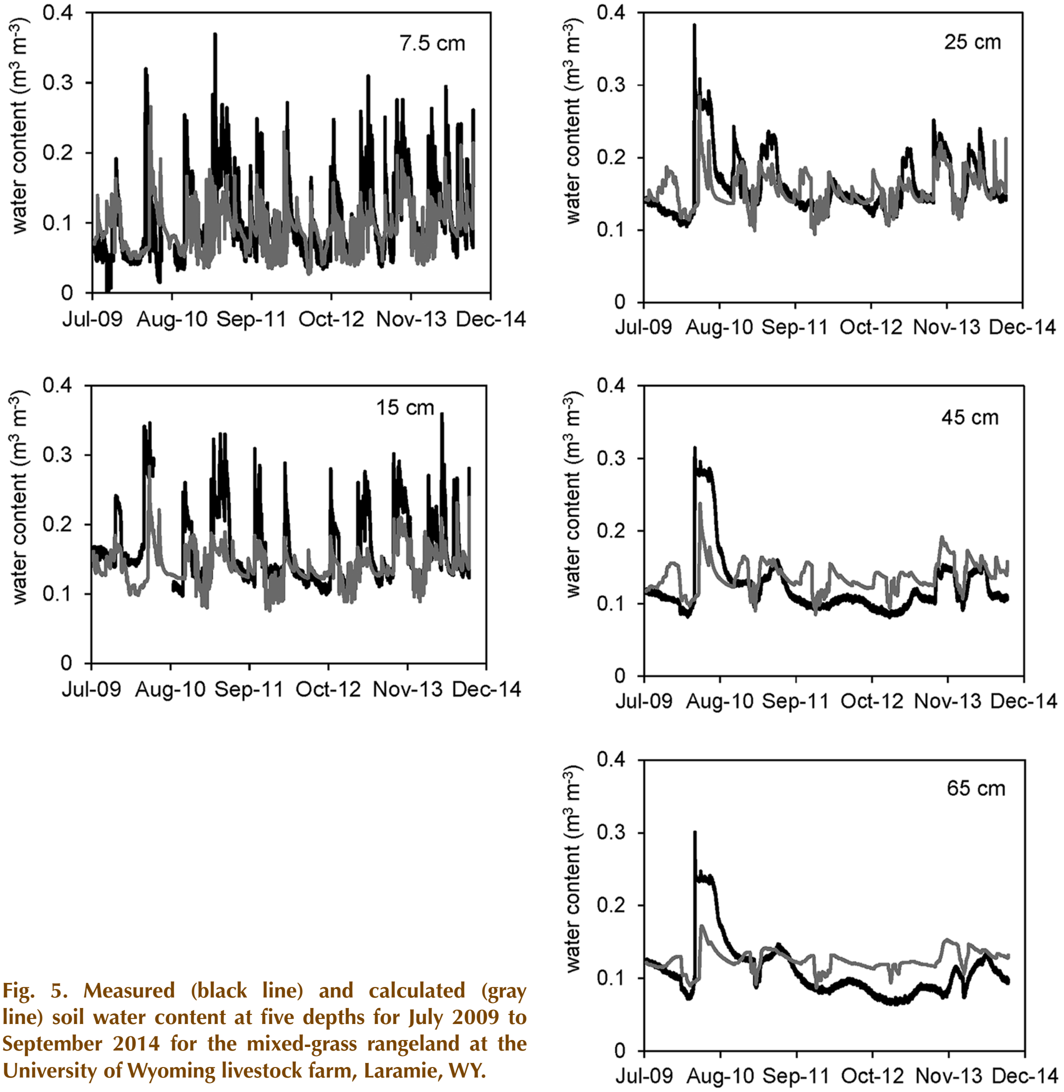

Fig. 5. Measured (black line) and calculated (gray line) soil water content at five depths for July 2009 to September 2014 for the mixed-grass rangeland at the University of Wyoming livestock farm, Laramie, WY.

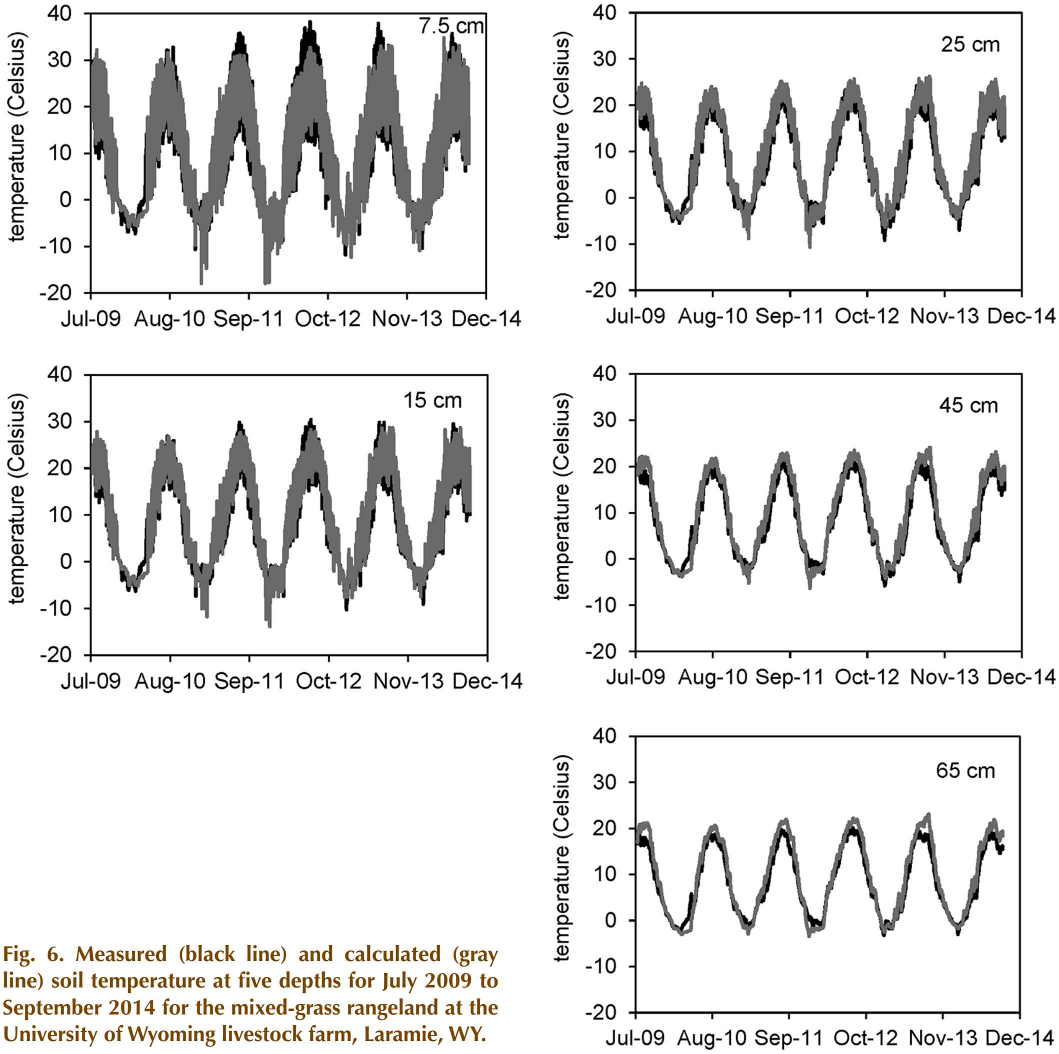

Fig. 6. Measured (black line) and calculated (gray line) soil temperature at five depths for July 2009 to September 2014 for the mixed-grass rangeland at the University of Wyoming livestock farm, Laramie, WY.

height (Fig. 7) was clearly underestimated for the 2009–2010 winter season during our earlier studies when the model did not yet include snow water vapor flow or the exponential within-canopy wind profile (Kelleners and Verma, 2012; Kelleners, 2013). The new model now accurately captures the significant difference in snowpack height and duration between the 2009–2010 season and the subsequent four winter seasons. This is attributed mainly to increased turbulent fluxes in the new model, which reduce the diurnal temperature fluctuations in the snow (results not shown). The remaining discrepancies between measured and calculated snow heights may be due to uncertainties in the amount of snowfall, the transient nature of snow cover at this site, and the absence of lateral redistribution due to blowing snow in the model. The calculated soil moisture and soil temperatures in the new model show only minor changes compared with the previous model results (see Kelleners, 2013).

SNOW-DOMINATED MOUNTAINOUS FOREST SOIL

Finally, the numerical model was applied to a mountainous forest soil in the Medicine Bow National Forest (locally known as Snowy Range), about 50 km west of Laramie, WY (elevation 3000 m above sea level; average annual air temperature 1.0°C; average annual precipitation 1.40 m). The soil is a loamy-skeletal, mixed Typic Dystrocryept on a south-facing slope with a slope angle of 12.5°. The soil is underlain by fractured bedrock starting at roughly the 0.6-m depth. The soil is heterogeneous, with many cobbles and tree roots. The soil physical characteristics are summarized in Table 5. The vegetation is dominated by Engelmann spruce (*Picea engelmannii* Parry ex. Engelm.) and subalpine fir [*Abies lasiocarpa* (Hook.) Nutt.]. Average tree height, stand stem biomass, and maximum stand LAI were estimated to be 20 m, 12 kg m^{-2}, and 5 m^2 m^{-2}, respectively (Jackson et al., 1996; Binkley et al., 2003). Relatively low values were chosen for stem biomass and LAI because the Medicine Bow forest is currently undergoing increased tree mortality due to a bark beetle epidemic.

Above-tree-level climate data for 15-min intervals were derived from 5-min weather data obtained from a Glacier Lakes Ecosystems Experiments Site (GLEES) tower, about 3 km to the northwest at 3200-m elevation (Frank et al., 2014). Precipitation was taken from the WY95 precipitation gauge at GLEES that measures both rain and snow. Atmospheric turbidity was estimated from average monthly values for Cheyenne,

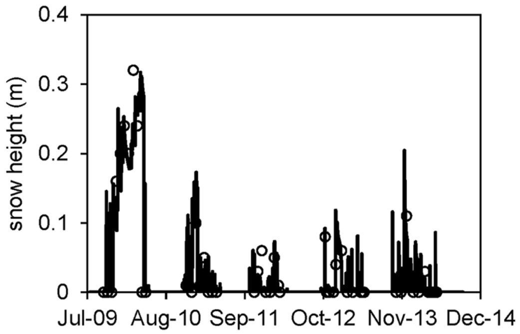

Fig. 7. Measured (symbols) and calculated (line) snow height for July 2009 to September 2014 for the mixed-grass rangeland at the University of Wyoming livestock farm, Laramie, WY.

WY, as presented by Curtis and Grimes (2004). Air temperature, relative humidity, atmospheric pressure, precipitation, and turbidity data were corrected for differences in elevation. The parameters in the Vrugt et al. (2001) root depth distribution function were $z_m = 0.6$ m, $P_z = 1$, and $z^* = 0.6$ m, resulting in a square-shaped distribution. Note that the maximum rooting depth for temperate coniferous forest averages 3.9 ± 0.4 m (Canadell et al., 1996) but that the bulk of the roots are mostly in the top 0.5 m of the soil (Jackson et al., 1996). The resulting distribution, with a high root concentration between 0 and 0.6 m and few roots between 0.6 and 3.9 m, cannot be captured accurately with the Vrugt et al. (2001) function, despite its versatility. We therefore elected to limit the modeled root zone to 0.6 m to at least capture the high root concentration in the top 0.6 m. The mass of roots, needed to calculate the root length density L, was estimated at 4.4 kg m^{-2} (Jackson et al., 1996).

The soil and underlying bedrock were modeled using four layers. The 0.6-m soil profile was described using three layers, each 20 cm in thickness. The underlying bedrock was described using one layer up to a depth of 10 m below the soil surface. A total of 81 nodes was used, with a grid spacing of 1 cm in the soil layers (requiring 60 nodes) and a gradually increasing grid spacing with depth of up to 2.1 m for the bedrock (requiring 21 nodes). Water retention for the three soil layers was determined at the University of Wyoming (Table 6). Water retention in the dry soil range was measured using a WP4 dew-point potentiometer (Decagon Devices). Water retention in medium wet soil ($-10 < h < -1$ m) was measured using a pressure plate apparatus (Dane and Hopmans, 2002c) and by subjecting Tempe cells to the pressure-outflow method (Dane and Hopmans, 2002a). Water retention in wet soils ($h > -1$ m) was measured using hanging water columns (Dane and Hopmans, 2002b). Repacked soil was used in all cases. Conversion of gravimetric to volumetric water contents was conducted using estimated dry bulk density values (mass of soil [<2-mm diameter] per field unit volume, Table 5) to scale the water retention data so that the model captured the field-measured volumetric soil water contents in the heterogeneous soil. The saturated soil hydraulic conductivity and pore connectivity values were estimated at 25 cm d^{-1} and 0.5, respectively. The hydraulic properties of the fractured bedrock in Table 6 were all estimated using a low value for porosity, a relatively high value for α (early air entry on drying), and a relatively high value for K_{whs} (pore connectivity = 0.5).

Table 4. Model statistics of root mean square error (RMSE) and modeling efficiency (ME) for soil water content, soil temperature, and snow height for July 2009 to September 2014 for the mixed-grass rangeland at the University of Wyoming livestock farm, Laramie, WY.

	Soil water content		Soil temperature		Snow height	
Depth	**RMSE**	**ME**	**RMSE**	**ME**	**RMSE**	**ME**
cm	m^3 m^{-3}		°C		m	
Surface					0.05	0.57
7.5	0.04	0.30	2.9	0.92		
15	0.04	0.20	2.4	0.94		
25	0.03	0.28	2.4	0.93		
45	0.04	0.12	2.1	0.93		
65	0.04	0.05	2.0	0.93		

Table 5. Measured soil texture (<2-mm diameter), estimated soil dry bulk density ρ_b (mass of soil [<2-mm diameter] per field unit volume), and soil class for the south-facing mountainous forest site in the Medicine Bow National Forest, about 50 km west of Laramie, WY.

Depth	Sand	Silt	Clay	ρ_b	Class
cm		%		g cm^{-3}	
0–20	50	37	13	1.0	loam
20–40	50	35	15	0.7	loam
40–60	41	40	19	1.2	loam

The simulation period covered August 2009 to September 2014. The top boundary condition in the model was again due to precipitation and the surface energy balance. The bottom boundary condition for water flow and heat transport was free drainage and a zero temperature gradient, respectively. Soil and snow monitoring at the site started in October 2009 when there was already some snow on the ground. The soil environment was monitored using HydraProbe impedance–temperature sensors at 10, 30, and 50 cm below the soil surface (Stevens Water Monitoring Systems). Snow height was monitored using a downward-facing SR50 acoustic distance sensor (Campbell Scientific). Initiating the simulation period in August instead of October has the benefit of well-defined soil conditions. At this stage in the season, the soil is generally dry and warm and the ice content is zero. Also, snow cover is unlikely. The initial soil conditions for August 2009 were estimated by using a preliminary model run and by taking the soil conditions for August 2014 as the initial conditions for August 2009.

Table 6. Residual water content θ_{wr}, porosity ϕ, the shape parameters α and n in the van Genuchten (1980) soil water retention function, and saturated hydraulic conductivity K_{whs} for the three soil layers and the underlying fractured bedrock at the south-facing mountainous forest site in the Medicine Bow National Forest, about 50 km west of Laramie, WY.

Depth	θ_{wr}	ϕ	α	n	K_{whs}
cm			cm^{-1}		cm d^{-1}
0–20	0.0	0.351	0.038	1.277	25
20–40	0.0	0.218	0.030	1.280	25
40–60	0.0	0.440	0.074	1.261	25
60–1000	0.0	0.050	0.100	1.500	700

Measured and calculated soil water content, soil temperature, and snow height are shown in Fig. 8, 9, and 10, respectively. The modeling statistics are summarized in Table 7. The ME values were highest for soil temperature ($0.85 \leq \text{ME} \leq 0.88$), intermediate for snow height (ME = 0.57), and lowest for soil water content ($0.06 \leq \text{ME} \leq 0.37$). The soils at this site are heterogeneous with many cobbles and large roots. It's therefore unrealistic to expect a perfect fit between measured and calculated soil water content. The relatively high RMSE values for soil water content, between 0.05 and 0.07 $m^3\ m^{-3}$, reflect this as well. Large systematic errors in the calculated soil water contents can be observed during the spring melt in April to May 2011 and April to May 2014 (Fig. 8). The measured water contents increased with time, presumably due to incoming meltwater from the overlying snowpack. In contrast, the calculated soil water contents decreased due to a combination of limited snow meltwater input and gradually increasing root water uptake. The calculated average snow temperature during these periods was −2 to −3°C, while the actual snowpack was probably isothermal.

The calculated snow height was significantly overestimated in the 2010–2011 winter. The overestimate was a little less severe than suggested by Fig. 10 because the actual snow height ex-

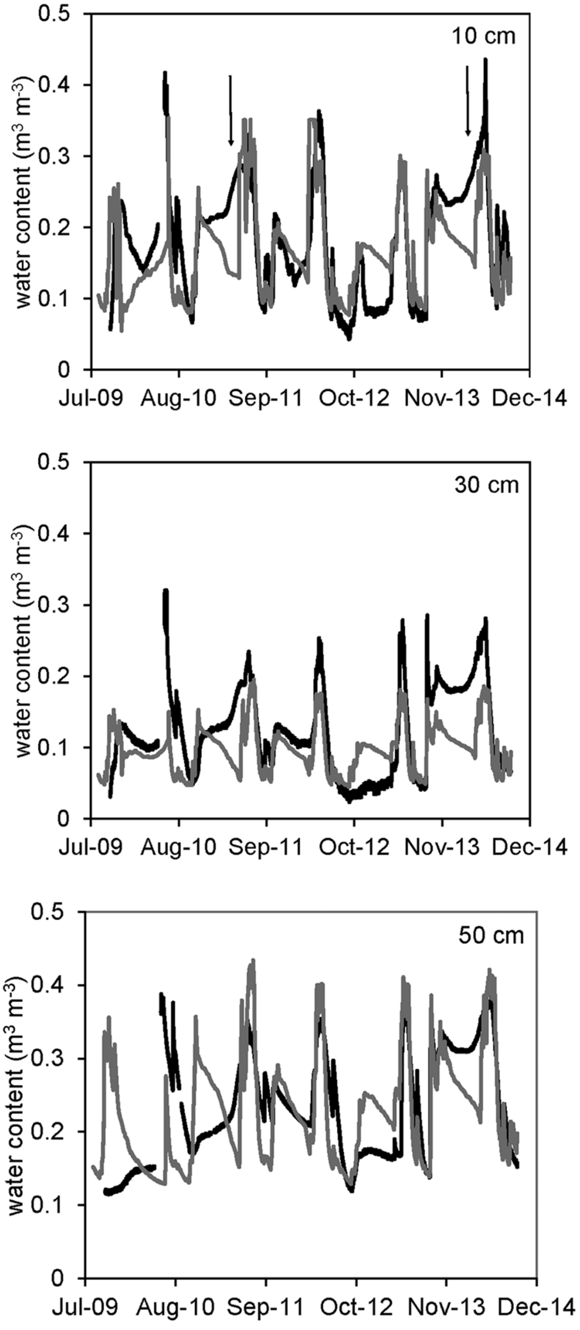

Fig. 8. Measured (black line) and calculated (gray line) soil water content at three depths for August 2009 to September 2014 for the south-facing mountainous forest site in the Medicine Bow National Forest, about 50 km west of Laramie, WY. The two vertical arrows in the top panel (10 cm) indicate April to May 2011 and April to May 2014, respectively, when soil water contents are significantly underestimated by the model.

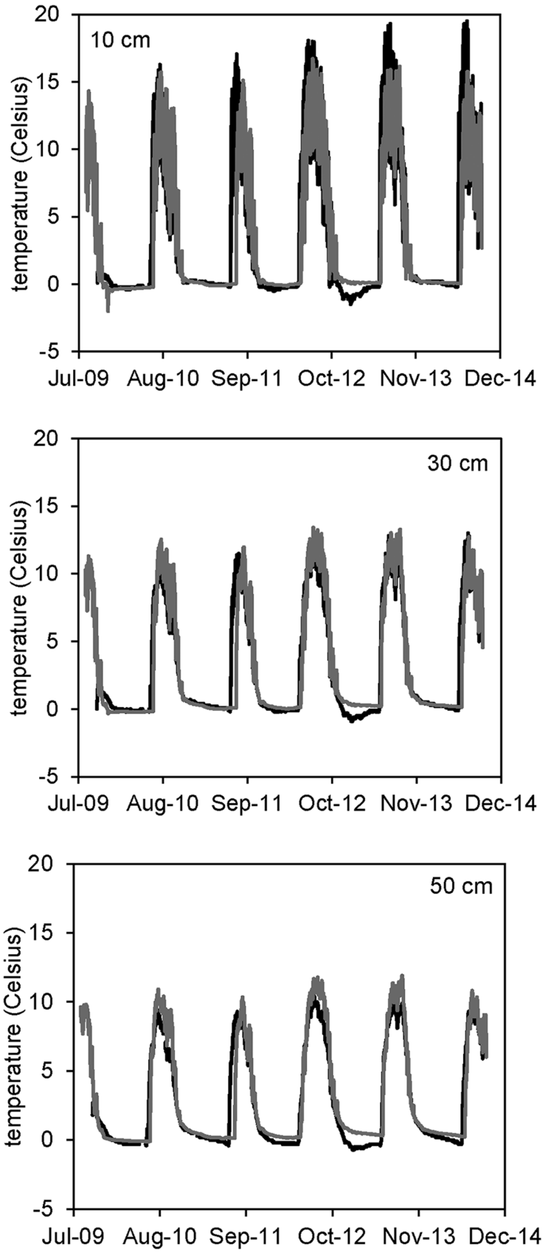

Fig. 9. Measured (black line) and calculated (gray line) soil temperature at three depths for August 2009 to September 2014 for the south-facing mountainous forest site in the Medicine Bow National Forest, about 50 km west of Laramie, WY.

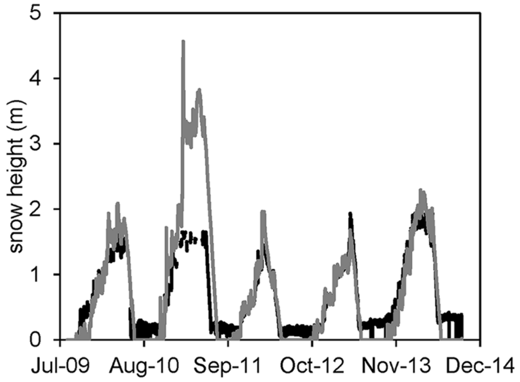

Fig. 10. Measured (black line) and calculated (gray line) snow height for August 2009 to September 2014 for the south-facing mountainous forest site in the Medicine Bow National Forest, about 50 km west of Laramie, WY.

ceeded the sensor height during this period, resulting in missing measured values. However, snow heights above 4 m probably did not occur. The high calculated snow heights are almost certainly due to the GLEES area, which served as the source for the precipitation data, receiving more snowfall than the study site. For example, a snow height of 3.8 m was measured manually at GLEES in April 2011. We applied a generic elevation correction to precipitation that did not capture the large differences in snow input between GLEES and our site during this event. Note that the non-zero height readings of up to 0.4 m during the summer periods are due to the acoustic sensor signal reflection of understory vegetation. The measured snow height was set to zero for the months of July and August for the calculation of RMSE and ME because snow cover is unlikely during these 2 mo. The understory vegetation was not simulated in the present model application.

Small systematic differences between measured and calculated soil temperatures can also be observed (Fig. 9). The calculated soil temperature at the 10-cm depth was often underestimated during the summer months. This may be due to the canopy energy balance method being used where Beer's law is used to calculate the fraction of solar radiation that is being intercepted by the canopy. In reality, portions of the solar radiation beam may reach the surface without being intercepted because the canopy is not completely closed. This results in some locations being warmer than expected. This type of overestimation is most likely in the summer when the sun is relatively high in the sky. Vegetation change due to the ongoing bark beetle epidemic may also be a contributing factor. The delay in calculated soil warmup in June and July 2011 for all depths is due to the delayed melt of the snowpack for the 2010–2011 winter owing to the likely overestimation of snowfall during February 2011, as mentioned above.

CONCLUSIONS

The numerical model for coupled water flow and heat transport in soil and snow was applied to a warm bare desert lysimeter soil, a cold mixed-grass rangeland soil, and a snow-dominated mountainous forest soil. The combined simulation periods totaled >14 yr. Results for the bare lysimeter soil showed that the lysimeter mass change due to incoming precipitation and outgoing evaporation, expressed as liquid water gain, was captured reasonably well by the model (measured gain = 111 mm; calculated gain = 95 mm; ME for bare soil evaporation = 0.41). The comparison of measured vs. calculated soil temperatures was hampered by the lysimeter design, which allows three-dimensional heat transport that deviates from the one-dimensional heat transport as assumed by the model. Model performance for soil temperature was best for the mixed-grass rangeland soil, with ME $\geq$ 0.92 for all five depths. The model's ability to simulate realistic snowpack heights was demonstrated for both the rangeland soil and the mountainous forest soil, where snow height was calculated with ME = 0.57 for both sites.

Table 7. Model statistics of root mean square error (RMSE) and modeling efficiency (ME) for soil water content, soil temperature, and snow height for August 2009 to September 2014 for the south-facing mountainous forest site in the Medicine Bow National Forest, about 50 km west of Laramie, WY.

	Soil water content		Soil temperature		Snow height	
Depth	**RMSE**	**ME**	**RMSE**	**ME**	**RMSE**	**ME**
cm	$m^3\ m^{-3}$		°C		m	
Surface					0.33	0.57
10	0.06	0.37	1.9	0.85		
30	0.05	0.24	1.5	0.88		
50	0.07	0.06	1.3	0.88		

Calculating realistic soil water contents is a challenge and ME values varied considerably in this study, with $0.32 \leq \text{ME} \leq 0.75$ for the bare soil, $0.05 \leq \text{ME} \leq 0.30$ for the rangeland soil, and $0.06 \leq \text{ME} \leq 0.37$ for the forest soil. Calculated water contents are sensitive to the prescribed soil water retention curves, which were measured in the laboratory. However, the translation to actual field conditions is challenging due to variations in gravel content (lysimeter soil), the presence of a dense $CaCO_3$ layer (rangeland soil), and the presence of cobbles and large roots (forest soil). The process of hysteresis and the presence of macropores (neither included in the model) further add to the challenge, as do uncertainties about soil water sensor calibration and the distribution and activity of roots. It's conceivable that the soil water ME values can be improved by optimizing the soil hydraulic (all three sites) and the vegetation parameters (rangeland and forest sites) using an inverse algorithm. This was beyond the scope of the current study but could be attempted in the future.

Overall, though, the model presented in this study was able to calculate realistic soil water contents for all three ecosystems. Advantages of the current model are the inclusion of all three water phases (ice, liquid, and vapor) in a physics-based approach, a realistic within-canopy exponential wind profile (Dolman, 1993), the inclusion of compensated root water uptake (de Jong van Lier et al., 2008), and the absence of an empirical reduction factor for soil evaporation (van de Griend and Owe, 1994; Tang and Riley, 2013). These attributes should allow application of the model to a variety of terrestrial ecosystems without the need for prior assumptions about the dominant processes. A disadvantage of the model is the computational effort required to solve the coupled water flow and heat transport equations, and research to solve these equations more efficiently is ongoing.

APPENDIX: DERIVATIVE TERMS

The derivative of liquid water content θ_w (m^3 m^{-3}) with respect to relative saturation S_e (dimensionless) for snow is

$$\frac{d\theta_w}{dS_e}=\frac{\left(1+S_eF_c-F_c\right)\left[1-F_c\theta_i\left(\rho_i/\rho_w\right)\right]}{\left(1+S_eF_c-F_c\right)^2}-\frac{F_c\left[S_e-S_eF_c\theta_i\left(\rho_i/\rho_w\right)+F_c\theta_i\left(\rho_i/\rho_w\right)\right]}{\left(1+S_eF_c-F_c\right)^2} \quad [A1]$$

where F_c is mass of liquid water that can be retained per mass of dry snow (kg kg^{-1}), θ_i is ice content (m^3 m^{-3}), ρ_i is ice density (kg m^{-3}), and ρ_w is liquid water density (kg m^{-3}). The derivative of soil water surface tension γ (kg s^{-2}) with respect to temperature T (°C) is (Bachmann and van der Ploeg, 2002)

$$\frac{d\gamma}{dT}=-0.0001535 \quad [A2]$$

The derivative of θ_w with respect to soil water pressure head h (m) is (Mous, 1995; Radcliffe and Šimůnek, 2010)

$$\frac{d\theta_w}{dh}=\begin{cases}\alpha^n\left(\phi-\theta_{wr}\right)mn\left(-h\right)^{n-1} \\ \quad\times\left[1+\left(-\alpha h\right)^n\right]^{-m-1}, & h<0 \\ \alpha m\left(\phi-\theta_{wr}\right)S_e^{1/m} \\ \quad\times\left(1-S_e^{1/m}\right)^m\left(1-m\right)^{-1}, & h\geq 0\end{cases} \quad [A3]$$

where α (m^{-1}), n (dimensionless), and m (dimensionless) are empirical parameters in the van Genuchten (1980) water retention function, ϕ is porosity (m^3 m^{-3}), and θ_{wr} is residual liquid water content (m^3 m^{-3}). The derivative of relative humidity H_r (dimensionless) with respect to h is given by

$$\frac{dH_r}{dh}=H_r\left[\frac{M_wg}{R\left(T+273.15\right)}+\frac{\phi}{\theta_w^2}M_wM\frac{d\theta_w}{dh}\right] \quad [A4]$$

where M_w is molecular mass of water (kg mol^{-1}), g is acceleration due to gravity (m s^{-2}), R is the gas constant (J mol^{-1} K^{-1}), and M is molality at saturation (mol kg^{-1} of solvent). The derivative of H_r with respect to T is

$$\frac{dH_r}{dT}=\begin{cases}0 & \text{snow} \\ H_r\left[\frac{-hM_wg}{R\left(T+273.15\right)^2}\right. \\ \quad\left.+\frac{\phi}{\theta_w^2}M_wM\frac{d\theta_w}{dT}\right] & \text{soil,}\quad h\leq 0\end{cases} \quad [A5]$$

The derivative of θ_w with respect to T is (Kelleners, 2013)

$$\frac{d\theta_w}{dT}=\begin{cases}\frac{-2a^2T}{\left(1+a^2T^2\right)^2}\frac{\theta_i\rho_i}{\rho_w}\left(1-\frac{1}{1+a^2T^2}\right)^{-2} & \text{snow, } T<0 \\ \left(\frac{\gamma_f}{g}\frac{1}{T+273.15}+\frac{\phi}{\theta_w}\frac{RM}{g}\right) \\ \times\left[\frac{dh}{d\theta_w}+\frac{\phi}{\theta_w^2}\frac{RM\left(T+273.15\right)}{g}\right]^{-1} & \text{soil, } T<0\end{cases} \quad [A6]$$

where a = 1000°C^{-1} is a constant with reported values of 100 to 1000°C^{-1} (Jordan et al., 1999), and γ_f is the latent heat of fusion (J kg^{-1}). Finally, $d\rho_{vs}/dT$ over ice and water is calculated using sixth-order polynomials and data provided by Oleson et al. (2013).

ACKNOWLEDGMENTS

The SEPHAS large weighing lysimeter study is based on work supported by the National Science Foundation under Grant no. EPS-0447416. The field measurements at the mixed-grass rangeland site were facilitated by an equipment grant from the University of Wyoming Agricultural Experiment Station. Field data collection and modeling work at the mountainous forest site was supported by a University of Wyoming Faculty Grant-In-Aid award and by the National Science Foundation funded Wyoming Center for Environmental Hydrology and Geophysics under Grant no. EPS-1208909. The comments of three anonymous reviewers and the associate editor helped to improve the paper.

REFERENCES

Augustine, J.A., G.B. Hodges, E.G. Dutton, J.J. Michalsky, and C.R. Cornwall. 2008. An aerosol optical depth climatology for NOAA's national surface radiation budget network (SURFRAD). J. Geophys. Res. 113:D11204. doi:10.1029/2007JD009504

Bachmann, J., and R.K. van der Ploeg. 2002. A review of recent developments in soil water retention theory: Interfacial tension and temperature effects. J. Plant Nutr. Soil Sci. 165:468–478. doi:10.1002/1522-2624(200208)165:4<468::AID-JPLN468>3.0.CO;2-G

Binkley, D., U. Olsson, R. Rochelle, T. Stohlgren, and N. Nikolov. 2003. Structure, production and resource use in some old-growth spruce/fir forests in the Front Range of the Rocky Mountains, USA. For. Ecol. Manage. 172:271–279. doi:10.1016/S0378-1127(01)00794-0

Canadell, J., R.B. Jackson, J.R. Ehleringer, H.A. Mooney, O.E. Sala, and E.D. Schulze. 1996. Maximum rooting depth of vegetation types at the global scale. Oecologia 108:583–595. doi:10.1007/BF00329030

Cass, A., G.S. Campbell, and T.L. Jones. 1984. Enhancement of thermal water vapor diffusion in soil. Soil Sci. Soc. Am. J. 48:25–32. doi:10.2136/sssaj1984.03615995004800010005x

Celia, M.A., E.T. Bouloutas, and R.L. Zarba. 1990. A general mass-conservative numerical solution for the unsaturated flow equation. Water Resour. Res. 26:1483–1496. doi:10.1029/WR026i007p01483

Chief, K., M.H. Young, B.F. Lyles, J. Healey, J. Koonce, E. Knight, et al. 2009. Scaling environmental processes in heterogeneous arid soils: Construction of large weighing lysimeter facility. Publ. 41249. Desert Res. Inst., Las Vegas, NV.

Colbeck, S.C. 1993. The vapor diffusion coefficient for snow. Water Resour. Res. 29:109–115. doi:10.1029/92WR02301

Colbeck, S.C., and G. Davidson. 1973. Water percolation through homogeneous snow. In: International Symposium on the Role of Snow and Ice in Hydrology, Banff, AB, Canada. Sept. 1972. IAHS Publ. 107. Inst. of Hydrology, Wallingford, UK. p. 242–256.

Curtis, J., and K. Grimes. 2004. Wyoming climate atlas. Wyoming State Climatologist Office, Laramie.

Dall'Amico, M., S. Endrizzi, S. Gruber, and R. Rigon. 2011. A robust and energy-conserving model of freezing variably-saturated soil. Cryosphere 5:469–484. doi:10.5194/tc-5-469-2011

Dane, J.H., and J.W. Hopmans. 2002a. Pressure cell. In: J.H. Dane and G.C. Topp, editors, Methods of soil analysis. Part 4. Physical methods. SSSA Book Ser. 5. SSSA, Madison, WI. p. 684–688. doi:10.2136/sssabookser5.4.c25

Dane, J.H., and J.W. Hopmans. 2002b. Hanging water column. In: J.H. Dane and G.C. Topp, editors, Methods of soil analysis. Part 4. Physical methods. SSSA Book Ser. 5. SSSA, Madison, WI. p. 680–683. doi:10.2136/sssabookser5.4.c25

Dane, J.H., and J.W. Hopmans. 2002c. Pressure plate extractor. In: J.H. Dane and G.C. Topp, editors, Methods of soil analysis. Part 4. Physical methods. SSSA Book Ser. 5. SSSA, Madison, WI. p. 688–690. doi:10.2136/sssabookser5.4.c25

de Jong van Lier, Q., D. Dourado Neto, and K. Metselaar. 2009. Modeling of transpiration reduction in van Genuchten–Mualem type soils. Water Resour. Res. 45:W02422. doi:10.1029/2008WR006938

de Jong van Lier, Q., J.C. van Dam, K. Metselaar, R. de Jong, and W.H.M. Duijnisveld. 2008. Macroscopic root water uptake distribution using a matric flux potential approach. Vadose Zone J. 7:1065–1078. doi:10.2136/vzj2007.0083

Dolman, A.J. 1993. A multiple-source land surface energy balance model for use in general circulation models. Agric. For. Meteorol. 65:21–45. doi:10.1016/0168-1923(93)90036-H

Duchon, C.E., and C.J. Biddle. 2010. Undercatch of tipping-bucket gauges in high rain rate events. Adv. Geosci. 25:11–15. doi:10.5194/adgeo-25-11-2010

Fayer, M.J. 2000. UNSAT-H Version 3.0: Unsaturated soil water and heat flow model: Theory, user manual, and examples. Rep. 13249. Pac. Northw. Natl. Lab., Richland, WA.

Farouki, O.T. 1981. The thermal properties of soils in cold regions. Cold Reg. Sci. Technol. 5:67–75. doi:10.1016/0165-232X(81)90041-0

Feddes, R.A., P.J. Kowalik, and H. Zaradny. 1978. Simulation of field water use and crop yield. Simul. Monogr. Pudoc, Wageningen, the Netherlands.

Flerchinger, G.N. 2000. The Simultaneous Heat and Water (SHAW) model: Technical documentation. Tech. Rep. 2000-09. Northw. Watershed Res. Ctr., Boise, ID.

Flerchinger, G.N., and K.E. Saxton. 1989. Simultaneous heat and water model of a freezing snow–residue–soil system: I. Theory and development. Trans. ASAE 32:565–571. doi:10.13031/2013.31040

Frank, J.M., W.J. Massman, B.E. Ewers, L.S. Huckaby, and J.F. Negron. 2014. Ecosystem CO_2/H_2O fluxes are explained by hydraulically limited gas exchange during tree mortality from spruce bark beetles. J. Geophys. Res. 119:1195–1215. doi:10.1002/2013JG002597

Fuchs, M., G.S. Campbell, and R.I. Papendick. 1978. An analysis of sensible and latent heat flow in a partially frozen unsaturated soil. Soil Sci. Soc. Am. J. 42:379–385. doi:10.2136/sssaj1978.03615995004200030001x

Green, I.R.A., and D. Stephenson. 1986. Criteria for comparison of single event models. Hydrol. Sci. J. 31:395–411. doi:10.1080/02626668609491056

Guymon, G.L., and J.N. Luthin. 1974. A coupled heat and moisture transport model for arctic soils. Water Resour. Res. 10:995–1001. doi:10.1029/WR010i005p00995

Hansson, K., J. Šimůnek, M. Mizoguchi, L.-C. Lundin, and M.Th. van Genuchten. 2004. Water flow and heat transport in frozen soil: Numerical solution and freeze–thaw applications. Vadose Zone J. 3:693–704. doi:10.2136/vzj2004.0693

Harlan, R.L. 1973. Analysis of coupled heat–fluid transport in partially frozen soil. Water Resour. Res. 9:1314–1323. doi:10.1029/WR009i005p01314

Jackson, R.B., J. Canadell, J.R. Ehleringer, H.A. Mooney, O.E. Sala, and E.D. Schulze. 1996. A global analysis of root distributions for terrestrial biomes. Oecologia 108:389–411. doi:10.1007/BF00333714

Jordan, R. 1991. A one-dimensional temperature model for a snow cover: Technical documentation for SNTHERM.89. Spec. Rep. 91-16. U.S. Army Corps Eng., Cold Regions Res. Eng. Lab., Hanover, NH.

Jordan, R.E., E.L. Andreas, and A.P. Makshtas. 1999. Heat budget of snow-covered sea ice at North Pole 4. J. Geophys. Res. 104:7785–7806. doi:10.1029/1999JC900011

Kammerer, G., R. Nolz, M. Rodny, and W. Loiskandl. 2014. Performance of Hydra probe and MPS-1 soil water sensors in topsoil tested in lab and field. J. Water Resour. Prot. 6:1207–1219. doi:10.4236/jwarp.2014.613110

Kelleners, T.J. 2013. Coupled water flow and heat transport in seasonally frozen soils with snow accumulation. Vadose Zone J. 12(4). doi:10.2136/vzj2012.0162

Kelleners, T.J., D.G. Chandler, J.P. McNamara, M.M. Gribb, and M.S. Seyfried. 2009. Modeling the water and energy balance of vegetated areas with snow accumulation. Vadose Zone J. 8:1013–1030. doi:10.2136/vzj2008.0183

Kelleners, T.J., and A.K. Verma. 2012. Modeling carbon dioxide production and transport in a mixed-grass rangeland soil. Vadose Zone J. 11(3). doi:10.2136/vzj2011.0205

Mahat, V., D.G. Tarboton, and N.P. Molotch. 2013. Testing above- and below-canopy representations of turbulent fluxes in an energy balance snowmelt model. Water Resour. Res. 49:1107–1122. doi:10.1002/wrcr.20073

Moene, A.F., and J.C. van Dam. 2014. Transport in the atmosphere–vegetation–soil continuum. Cambridge Univ. Press, New York.

Moldrup, P., T. Oleson, T. Yamaguchi, P. Schjonning, and D.E. Rolston. 1999. Modeling diffusion and reaction in soils: IX. The Buckingham–Burdine–Campbell equation for gas diffusivity in undisturbed soil. Soil Sci. 164:542–551. doi:10.1097/00010694-199908000-00002

Mous, S.L.J. 1995. An efficient solution procedure for the one-step experiment. Appl. Math. Model. 19:130–132. doi:10.1016/0307-904X(94)00006-R

Mualem, Y. 1976. A new model for predicting the hydraulic conductivity of unsaturated porous media. Water Resour. Res. 12:513–522. doi:10.1029/WR012i003p00513

Nassar, I.N., and R. Horton. 1989. Water transport in unsaturated nonisothermal salty soil: II. Theoretical development. Soil Sci. Soc. Am. J. 53:1330–1337. doi:10.2136/sssaj1989.03615995005300050005x

Nassar, I.N., and R. Horton. 1992. Simultaneous transfer of heat, water, and solute in porous media: I. Theoretical development. Soil Sci. Soc. Am. J. 56:1350–1356. doi:10.2136/sssaj1992.03615995005600050004x

Oleson, K.W., D.M. Lawrence, G.B. Bonan, B. Drewniak, M. Huang, C.D. Koven, et al. 2013. Technical description of Version 4.5 of the Community Land Model (CLM). Tech. Note TN-503+STR. Natl Ctr. Atmos. Res., Boulder, CO.

Or, D., P. Lehmann, E. Shahraeeni, and N. Shokri. 2012. Advances in soil evaporation physics: A review. Vadose Zone J. 12(4). doi:10.2136/vzj2012.0163

Painter, S.L. 2011. Three-phase numerical model of water migration in partially frozen geological media: Model formulation, validation, and applications. Comput. Geosci. 15:69–85. doi:10.1007/s10596-010-9197-z

Philip, J.R., and D.A. de Vries. 1957. Moisture movement in porous materials under temperature gradients. Trans. Am. Geophys. Union 38:222–232. doi:10.1029/TR038i002p00222

Pinzer, B.R., M. Schneebeli, and T.U. Kaempfer. 2012. Vapor flux and recrystallization during dry snow metamorphism under a steady temperature gradient as observed by time-lapse micro-tomography. Cryosphere 6:1141–1155. doi:10.5194/tc-6-1141-2012

Radcliffe, D.E., and J. Šimůnek. 2010. Soil physics with HYDRUS: Modeling and applications. CRC Press, Boca Raton, FL.

Russo, D. 1983. Leaching characteristics of a stony desert soil. Soil Sci. Soc. Am. J. 47:431–438. doi:10.2136/sssaj1983.03615995004700030008x

Saito, H., J. Šimůnek, and B.P. Mohanty. 2006. Numerical analysis of coupled water, vapor, and heat transport in the vadose zone. Vadose Zone J. 5:784–800. doi:10.2136/vzj2006.0007

Šimůnek, J., M. Sejna, H. Saito, M. Sakai, and M.Th. van Genuchten. 2013. The HYDRUS-1D software package for simulating the one-dimensional movement of water, heat, and multiple solutes in variably-saturated media. Version 4.16. Univ. of California, Riverside.

Shimizu, H. 1970. Air permeability of deposited snow. Contrib. 1053. Inst. Low Temp. Sci., Sapporo, Japan.

Tang, J.Y., and W.J. Riley. 2013. A new top boundary condition for modeling surface diffusive exchange of a generic volatile tracer: Theoretical analysis and application to soil evaporation. Hydrol. Earth Syst. Sci. 17:873–893. doi:10.5194/hess-17-873-2013

Tarboton, D.G., and C.H. Luce. 1996. Utah energy balance snow accumulation and melt model (UEB): Computer model technical description and users guide. Utah Water Res. Lab., Logan.

van de Griend, A.A., and M. Owe. 1994. Bare soil surface resistance to evaporation by vapor diffusion under semiarid conditions. Water Resour. Res. 30:181–188. doi:10.1029/93WR02747

van Genuchten, M.Th. 1980. A closed-form equation for predicting the hydraulic conductivity of unsaturated soils. Soil Sci. Soc. Am. J. 44:892–898. doi:10.2136/sssaj1980.03615995004400050002x

Vrugt, J.A., J.W. Hopmans, and J. Šimůnek. 2001. Calibration of a two-dimensional root water uptake model. Soil Sci. Soc. Am. J. 65:1027–1037. doi:10.2136/sssaj2001.6541027x

Zhao, L., D.M. Gray, and D.H. Male. 1997. Numerical analysis of simultaneous heat and mass transfer during infiltration into frozen ground. J. Hydrol. 200:345–363. doi:10.1016/S0022-1694(97)00028-0